IDENTIFICATION OF FORCE COEFFICIENTS IN TWO SQUEEZE FILM

DAMPERS WITH A CENTRAL GROOVE

A Thesis

by

SANJEEV SESHAGIRI

Submitted to the Office of Graduate Studies of
Texas A&M University
in partial fulfillment of the requirements for the degree of

MASTER OF SCIENCE

May 2011

Major Subject: Mechanical Engineering

IDENTIFICATION OF FORCE COEFFICIENTS IN TWO SQUEEZE FILM

DAMPERS WITH A CENTRAL GROOVE

A Thesis

by

SANJEEV SESHAGIRI

Submitted to the Office of Graduate Studies of
Texas A&M University
in partial fulfillment of the requirements for the degree of

MASTER OF SCIENCE

Approved by:

Chair of Committee,	Luis San Andrés
Committee Members,	Alan Palazzolo
	Luciana Barroso
Head of Department,	Dennis O'Neal

May 2011

Major Subject: Mechanical Engineering

ABSTRACT

Identification of Force Coefficients in Two Squeeze Film Dampers

with a Central Groove. (May 2011)

Sanjeev Seshagiri, B.E., R.V.College of Engineering

Chair of Advisory Committee: Dr. Luis San Andrés

Squeeze Film Dampers (SFD) provide viscous damping in rotor bearing systems to reduce lateral vibration amplitudes and to isolate mechanical components. Aircraft engine shafts, often supported on roller bearings, operate at high rotational speeds and are susceptible to large amplitude shaft whirl due to rotor imbalance. SFDs aid to reduce such large whirl amplitudes while also eliminating rotor instabilities.

The current work quantifies experimentally the forced performance of two parallel squeeze SFDs separated by a central groove. Force coefficients are identified in a specialized SFD test rig constructed to undergo similar operating and loading conditions as in jet engines. Of interest is to quantify the effect of a central feed groove on the forced performance of SFDs and to validate predictions from a computational tool. The test rig comprises of an elastically supported bearing structure and one of two journals. Tests are conducted on two open ends SFDs, both with diameter D and nominal radial clearance c; each damper with two parallel film land lengths $L = {}^1\!/_5\, D$ and $2L$, separated by a feed groove of width L and depth $\frac{3}{4}\, L$. ISO VG 2 grade lubricant oil flows into the central groove via 3 orifices, 120° apart, and then through the film lands to finally exit to ambient. In operation, a static loader pulls the bearing to various static off center positions with respect to the stationary journal, and electromagnetic shakers (2,200 N) excite the test system with single frequency loads over a frequency range to generate rectilinear, circular and elliptical orbits with specified motion amplitudes. A frequency domain method identifies the SFD mechanical parameters, viz., stiffness, damping, and added mass coefficients.

The long damper generates 7 times more direct damping and 2 times more added mass compared to the short length damper. The damping coefficients are sensitive to the static eccentricity (up to 50% c) while showing lesser dependency on the amplitude of whirl motion (up to 20% c). On the other hand, added mass coefficients are nearly constant with static eccentricity and decrease with higher amplitudes of motion. The magnitudes of identified cross-coupled coefficients are insignificant for all imposed operating conditions for either damper.

Large dynamic pressures recorded in the central groove demonstrate the groove does not isolate the film lands by merely acting as a source of lubricant, but contributes to the generation of large added mass coefficients. The recorded dynamic pressures in the film lands and central groove do not evidence lubricant vapor or gas cavitation for the tested static eccentricities and amplitudes of motion.

The direct damping coefficients for both dampers are independent of excitation frequency over the frequency range of the tests. Predictions derived from a novel SFD computational tool that includes flow interactions in the central groove and oil supply orifices agree well with the experimental force coefficients for both dampers.

The current work advances the state of the art in SFDs for jet engines.

DEDICATION

Dedicated to my father, mother and sister

ACKNOWLEDGEMENTS

NOMENCLATURE

$a_{X(t)}, a_{Y(t)}$	BC accelerations along X and Y directions [m/s^2]
c	Nominal radial clearance [m]
c_A, c_B	Measured radial clearance of damper with Journal A and B [m]
$C_{\alpha\beta, (\alpha,\beta= X,Y)}$	SFD damping coefficients [Ns/m]
C^*	Predicted direct damping coefficients from classical lubrication analysis [Ns/m] , Eq.(26)
C_T, C_B	Hydraulic conductances of the top and bottom dampers [LPM/bar]
$(\bar{C}_{XX}, \bar{C}_{YY})_{SFD}$	Normalized (dimensionless) SFD direct damping coefficients ($=C/C^*$)
$(C_S)_{\alpha\beta,(\alpha,\beta= X,Y)}$	Identified remnant damping coefficients of the dry structure [Ns/m]
$(C_{SA})_{\alpha\beta}, (C_{SB})_{\alpha\beta}$ $(\alpha,\beta= X,Y)$	Identified remnant damping coefficients of the long and short length damper dry structures [N/m]
d_G	Physical (actual) groove depth [m]
d_η	Effective groove depth [m]
D	Journal diameter [m]
e_S	BC static eccentricity and along 45° [m]
e_X, e_Y	BC eccentricity along X and Y axes [m]
f_n	Natural frequency of the test system, dry or lubricated [Hz] ($=\omega_n/2\pi$)
f_{start}, f_{end}	Start and end frequencies for parameter fit [Hz]
$F_{X(t)}, F_{Y(t)}$	Applied shaker loads along X and Y directions [N]
$G_{\alpha\beta, (\alpha,\beta=X,Y)}$	Flexibility functions [m/N]
h	Lubricant film thickness [m]
$H_{(\omega)}$	Impedance function [N/m]
$K_{S\alpha}^{static}{}_{,(\alpha=A,B)}$	Static stiffness of the dry structures A and B [N/m]
$(K_S)_{\alpha\beta,(\alpha,\beta= X,Y)}$	Identified structural stiffness coefficients of the dry structure [N/m]
$(K_{SA})_{\alpha\beta}, (K_{SB})_{\alpha\beta}$ $(\alpha,\beta= X,Y)$	Identified structural stiffness coefficients of the long and short length damper dry structures [N/m]
L	Land length [m]
L_G	Central groove depth [m]

M	SFD added mass coefficients [kg]
M^{*}	Predicted direct added mass coefficients from classical lubrication analysis [kg], Eq.(26)
M_{BC}, M_{BC}^{eff}	Measured mass of BC and effective mass of BC [kg]
$(\bar{M}_{XX}, \bar{M}_{YY})_{SFD}$	Normalized (dimensionless) SFD direct damping coefficients (=M/M^*)
$(Mr_S)_{\alpha\beta,(\alpha,\beta=X,Y)}$	Identified residual masses of the dry structure [kg]
$(M_S)_{\alpha\beta,(\alpha,\beta=X,Y)}$	Identified inertia coefficients of the dry structure [kg]
P	Dynamic pressure in film land [bar]
P_a, P_{cav}	Ambient pressure and lubricant cavitation pressure [bar]
P_{in}, P_G	Lubricant pressures at journal inlet and in the central groove [bar]
$Q_{in}, Q_{out}, Q_T, Q_B$	Lubricant flow rates: Inlet, outlet, top damper, bottom damper [LPM]
r	Amplitude of circular motion [m]
R	Journal radius [m] (=$D/2$)
Re_*	Modified squeeze film Reynolds number, $\rho\omega c^2/\mu$
R_T, R_B	Hydraulic resistances of the top and bottom damper film lands [LPM/bar]
t	Time [s]
T, T_{supply}	Lubricant temperature and lubricant inlet temperature [^{o}C]
T_p	Period of single frequency whirl motion [=$2\pi/\omega$]
U_C, U_K, U_M	Uncertainties in damping [Ns/m], stiffness [N/m] and inertia [kg] coefficients
U_δ, U_ω	Uncertainties in measurement of displacement [m] and frequency [Hz]
V	Known volume of the oil collector tray [liters]
$X_{(t)}, Y_{(t)}$	BC displacements along X and Y directions [m]
δ	General notation for BC displacements (used in uncertainty analysis) [m]
$\Delta X, \Delta Y$	Amplitude of elliptical orbits along X and Y axes
ζ, ζ_S	Damping ratios of the lubricated and dry system
θ, Θ	Angular coordinates to specify angular locations on the BC [degrees]

ρ	Lubricant density [kg/m^3]
μ	Lubricant dynamic viscosity [Pa.s]
ω, ω_n	Excitation frequency, natural frequency [rad/s]

Matrices and Vectors

a	Vector of BC accelerations in the time domain [m/s^2]
$\overline{\mathbf{a}}$	Discrete Fourier Transform (DFT) of time domain BC accelerations [m/s^2]
A	Matrix of stacked real and imaginary parts of flexibility functions at each frequency ω [N/m]
$\mathbf{C_S}, \mathbf{C}, \mathbf{C_{SFD}}$	Matrices of damping coefficients of dry structure, lubricated system and squeeze film [Ns/m]
$\mathbf{F_1}, \mathbf{F_2}, \mathbf{F}_{(t)}$	Vectors of applied forces in time domain on support structure [N]
$\overline{\mathbf{F}}_{(\omega)}$	Discrete Fourier Transform (DFT) of applied force vectors [N]
$\overline{\mathbf{F}}_{e(\omega)}$	Reduced force vector ($\overline{\mathbf{F}}_{(\omega)}$ - $M_{BC}\overline{\mathbf{a}}$) [N]
$\mathbf{G}, \mathbf{G_{dry}}$	Flexibility functions of the lubricated and dry systems [m/N]
$\mathbf{H}, \mathbf{H_{dry}}$	Impedance functions of the lubricated and dry systems [N/m]
I	Identity matrix
$\mathbf{K_S}, \mathbf{K}, \mathbf{K_{SFD}}$	Matrices of stiffness coefficients of dry structure, lubricated system and squeeze film [N/m]
$\mathbf{M_S}, \mathbf{M}, \mathbf{M_{SFD}}$	Matrices of inertia coefficients of dry structure, lubricated system and squeeze film [kg]
z	Vector of BC displacements in the time domain [m]
$\overline{\mathbf{z}}_{(\omega)}$	Discrete Fourier Transform (DFT) of time domain BC displacements [N]

Subscripts

k	Frequency index for single frequency excitation

TABLE OF CONTENTS

LIST OF TABLES

LIST OF FIGURES

Page

CHAPTER I

INTRODUCTION

Squeeze Film Dampers (SFD) are used in rotating machinery to attenuate rotor synchronous response and suppress subsynchronous rotordynamic instabilities [1]. SFDs are widely employed in aircraft gas turbine engines to provide external damping to roller bearings that support the engine shaft. Figure 1 illustrates a typical SFD configuration consisting of an oil film contained between housing and a nonrotating journal. The journal, typically the outer race of a roller bearing, is restrained from rotation by using a pin. The oil film is maintained by a continuous supply of pressurized lubricant through feed holes in the housing. As the inner race of the ball bearing spins with the shaft, the shaft and outer race together whirl within the housing, thus squeezing the oil film. Dynamic pressures generated by squeezing action of lubricant result in forces that serve to damp excessive whirl motion amplitudes of the shaft.
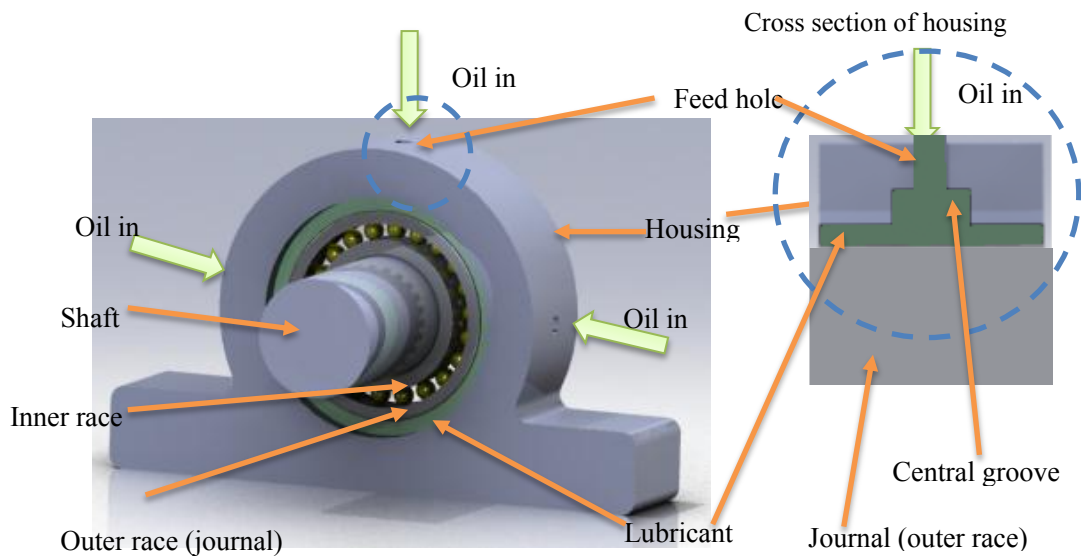
Figure 1. Depiction of a squeeze film damper with a central groove

_____

This thesis follows the style of Transactions of the ASME.

The magnitude of damping offered by a squeeze film damper depends on its geometry, presence of supply and discharge grooves, lubricant feed pressure and feeding arrangement, oil viscosity and density, type of journal motion and occurrence of air ingestion and cavitation [1]. The effects of geometry, oil feeding arrangements and end seals have not been thoroughly researched.

A central feeding groove affects the available damping and significantly increases the added mass coefficients arising from the lubricant [2]. Users typically regard a groove as a constant pressure region not affecting the SFD forced response. However, experiments have consistently demonstrated otherwise [3]. Delgado and San Andrés [4] develop a finite element procedure to predict force coefficients of a grooved SFD that show the best correlation to test data, to date.

Air ingestion is of special interest since it degrades SFD forced performance. Ambient air ingested into the lubricant film at high excitation frequencies and with large amplitudes of motion reduces the direct damping available from the SFD.

The project sponsor intends to investigate new squeeze film damper designs in its efforts to develop advanced gas turbine engines. The sponsor is interested in benchmarking SFD forced performance and developing an improved SFD computational tool validated against experimental data. The proposed work aims to achieve the sponsor objectives by identifying force coefficients from measurements made on various configurations of a squeeze film damper test rig. The test results will advance the art in SFDs for jet engines [5].

CHAPTER II

LITERATURE REVIEW

This section reviews past literature related to the parameter identification of SFDs with feed grooves. The first paragraphs briefly describe past work in parameter identification methods, including the IVF method that will be used in the proposed work. The ensuing paragraphs review papers that report experimental parameters in SFD with feed grooves. The final section reviews some relevant papers that identify parameters in simple SFD geometries using various types of dynamic loads, including operation with two-phase phenomena like air entrainment and vapor cavitation.

Della Pietra and Adiletta [6] review comprehensively SFD research conducted since the 1960s and present the chief findings. The authors discuss SFD configurations, operating conditions and flow regimes, and modeling of SFD forces and film pressures. Analytical developments and their validation with test data are also discussed.

Tiwari, Lees and Friswell [7] review time and frequency domain methods used to identify bearing parameters and provide a chronological list of parameter identification techniques developed over the past 50 years. The basic concepts, assumptions and governing equations of bearing models are listed and the parameter identification algorithms are explained. The reviewed identification methods are classified based on the type of excitation delivered to the test system viz., static and dynamic loads.

Fritzen [8] devises the Instrumental Variable Filter Method (IVFM), an improvement over the least squares method, to identify parameters in mechanical systems. The iterative IVFM starts with stiffness, damping and mass matrices (**K, C, M)** identified by the least squares method and builds a new instrument variable matrix **W**. Since **W** is free from measurement noise, each iteration delivers better estimates of **K, C, M** and the iteration ends when a specified error tolerance is reached. The method rejects measurement noise in the signals and the IVF delivered coefficients are better estimated compared to the least squares method [9].

II.1 Literature on SFDs with feed grooves and the effect of fluid inertia

Tichy [10] derives analytically the dynamic pressure field in open ends and sealed squeeze film dampers using the modified Reynolds equation, for cases with and without fluid inertia considered. Fluid inertia causes a significant increase in pressure amplitudes and phase shift. The shapes of the dynamic pressures change notably with static eccentricity. Increases in static eccentric position cause a decrease in phase shift of the pressures at different Reynolds numbers but an increase in pressure amplitudes.

San Andrés [2] presents a analysis in which the fluid in a feed groove is considered as slightly compressible. The analysis uses the short length bearing model and is valid only for small amplitude journal motions. Based on previous experimental evidence, dynamic pressures in the central groove are not considered to be nil. The dynamic pressures in the groove are obtained by applying mass flow balance and appropriate boundary conditions to the fluid bulk flow equations. Predictions show excellent agreement with experimental data for a SFD with a shallow groove of depth equal to twice the radial clearance, tested by Ramli *et al.* [11], hence evidencing that a shallow groove SFD behaves as a single contiguous damper of effective length equal to the sum of land lengths and groove width.

Zhang and Roberts [12] predict force coefficients in an open ends SFD with a shallow feed groove. The analysis considers flow and pressure balance through the lubricant delivery system, central groove and film lands. Predictions of SFD inertia and damping force coefficients obtained from the analysis are compared with test data in [13] and [14]. The comparisons reveal that predicted damping coefficients match well with experimental data but the added mass coefficients are underpredicted by a factor of 2 for low static eccentricities. The discrepancy increases with higher eccentricities.

Arauz and San Andrés [15] measure dynamic fluid pressures in the land and feed groove of an open ends SFD performing circular centered orbits. Recorded fields fields for two groove-to-land clearance ratios (c_g/c) equaling 5 and 10 are integrated to determine radial and tangential forces. Arauz and San Andrés [3] further demonstrate experimentally, the effect of a feed groove on the forced response of an open end SFD

and a sealed SFD. Tests are conducted with two groove depths and orbit radii equal to 25% and 50% of the radial clearance. Significant dynamic pressures in the groove that are 90° out of phase with the pressures in the film land evidence the inertial nature of the groove pressures. The authors note that the dynamic pressure in the groove is the same order of magnitude as in the lands, showing that the groove is not merely a source of lubricant. The tangential (damping) forces derived from the dynamic pressures in the land and groove are also of similar magnitude, showing that the groove generates significant damping which adds to the damping forces arising from the lands. The forces increase with decrease in (c_g/c) ratio, implying that shallower grooves aid to generate higher dynamic forces.

Qingchang et al. [16] derive an equation for the unbalance response of a rotor supported in SFDs. Qingchang *et al.*[17] determine analytically the effect of a groove on SFD forced response. The groove and film lands are analyzed separately using the Navier-Stokes equations and the results are combined to describe the overall SFD forced response. Increase in depth of the circumferential feed groove results in an increase in whirl orbit radius, demonstrating that feed grooves act to decrease the vibration attenuation capability of a SFD. For cavitated film condition operating with high Reynolds number, the effect of groove on the imbalance response of the rotor is negligible. The authors conclude that the groove generates appreciable tangential forces compared to the radial forces. On the contrary, literature evidences that grooves do generate large radial forces, and hence a large fluid inertia effect. The predicted damping coefficients are in good agreement with test data for orbit radii up to 60% of the radial clearance, while added mass coefficients are poorly predicted.

Lund *et al*. [18] solve a first-order Reynolds equation using small-amplitude motion perturbation about a static equilibrium position of the journal. A bulk flow model describes the fluid conditions in the central groove. Flow balance between the damper and lands forms the basis of a differential equation for the groove pressure, which is solved by perturbation. Integration of the groove pressures yield damping and inertia coefficients. The authors describe a test rig with end seals used to verify the predictions

from the developed analytical method but do not present a comparison of experimental data with predictions.

Kim and Lee [19] analyze dynamic pressure fields in a centered SFD with a feed groove at its mid-plane and identify its dynamic characteristics. The analysis considers effect of single and two stage seals. The analysis reveals that the pressure levels in the SFD with a two stage seal is higher than with a single stage seal. Experimental damping and added mass coefficients are identified in a SFD test rig with a two-stage seal while varying seal clearances. Comparison of test data to predictions show that the added mass coefficients are predicted well but damping coefficients are overpredicted.

Defaye *et al.*[20] obtain experimental radial and tangential SFD forces in a sealed ends SFD for different oil feeding arrangements, locations of groove, oil feed pressures and temperatures. A SFD with a central oil supply groove generates the lowest tangential (damping) forces, while another SFD with three radial orifice feed holes supplying oil directly into the lands generates the highest damping forces. The lubricant cavitates at lower motion amplitudes in a SFD with feed orifices than one with a central supply groove since a central groove provides a more equalized feed pressure distribution. An eccentric groove that is offset from the damper mid-plane disturbs the SFD pressure field to a lesser extent than a centrally located groove, hence generating larger damping forces. Dynamic pressures measured in the feed groove are comparable in magnitude to those in the film lands, implying that a central groove plays a significant role in SFD forced performance. The groove pressures are out of phase by 180° with respect to the land pressures, and are hence of an inertial nature.

Arghir *et al.*[21] predict SFD pressures and resulting forces using a finite volume solution to bulk-flow equations. A comparison of squeeze film pressure predictions from the bulk-flow model with results from a 3D CFD simulation evidences that the bulk flow model performs well for low to medium modified squeeze film Reynolds numbers (Re_*) but becomes invalid at $Re_* > 50$. Note that $Re_*=\rho\omega c^2/\mu$, where (ρ,μ) are the lubricant density and viscosity, and (ω, c) are the operating frequency and the damper film radial clearance, respectively. The finite volume method involves

discretization of the damper into multiple cells, ensuring that cell faces coincide with the groove boundaries to prevent numerical discontinuities. Circumferential pressure fields exhibit peaks at the angular locations of feed orifices. Orifices can act not only as a lubricant source, but also as a sink. A feed groove smooths the pressure field. SFD radial and tangential forces obtained from integrating the bulk-flow pressure fields compare much better with test data obtained by Defaye *et al*. [20] than those obtained by solving the Reynolds equation alone.

II.2 Literature pertaining to parameter identification in simple SFD geometries

San Andrés and De Santiago [22] identify force coefficients in an open ends damper undergoing large amplitude circular and elliptical motions, up to 80% of the clearance. The damping coefficients along the principal directions (*X* and *Y*) from circular orbits are identical and increase with orbit amplitude. In the case of elliptical orbits, damping coefficients are identical for small amplitude motions. As the amplitude of motion increases, the damping coefficient along the major axis of motion grows. The fluid inertia coefficients are invariant for small amplitude motions, regardless of the orientation of ellipse with respect to the *X* and *Y* axes. Identified damping coefficients agree well with predictions based on a short bearing model if an effective land length between 78% and 82% of the actual land length is used.

San Andrés and Delgado [23] perform unidirectional load tests to identify damping and inertia coefficients in a SFD with an end seal. The SFD has an inlet groove and an exit recirculation groove with 4 orifice discharge ports. The seal dry friction force is identified first, followed by lubricated system coefficients. SFD damping coefficients are obtained by subtracting from the system coefficients, the effective damping arising from the mechanical seal. The test results show large system viscous damping coefficients at low frequencies and for small amplitudes of motion, evidencing the dominant effect of dry friction arising from the mechanical end seal. The film damping coefficients are nearly independent of whirl frequency, increasing slightly with the amplitude of motion. Predictions of damping based on the short length bearing model

agree well with test data. On the other hand, predictions of inertia coefficients match test data if twice the land length is used in the classical prediction formulae.

San Andrés and Delgado [24] perform circular center orbit tests to identify the mechanical parameters of a SFD with a mechanical seal. The identified viscous damping from the squeeze film is independent of frequency and increases with amplitude of orbital motion. The experimental damping coefficients agree well with predictions based on the short bearing model. The added mass coefficients agree with predictions if twice the land length is used in the predictive relation.

Adiletta and Della Pietra [25] measure dynamic pressure fields at three angular positions at the mid-section of a SFD describing circular orbits about static off-centered positions. Pressure data is acquired for varying supply pressures and whirl frequencies. The experimental pressure data match theoretical predictions for a full film condition, particularly at low static eccentricities, provided the level of supply pressure is adequate. During cavitated operation, film rupture is preceded by tensile stresses in the lubricant as evidenced by the test data.

Diaz and San Andrés [26] demonstrate the differences between lubricant vapor cavitation and air entrainment through controlled motion tests on a squeeze film damper for two conditions; flooded plenum and plenum vented to ambient. Dynamic pressure measurements are made at various locations in the film lands while the rotor whirls with circular centered orbit of amplitude equal to 50% of the film clearance. Dynamic pressure fields with flooded plenum show a flat region at the instant when film thickness is maximum, evidencing vapor cavitation. For operation with plenum vented to ambient, high frequency spikes in the pressure signals that differ markedly for each period of journal motion indicate air entrainment. A rapid decrease in tangential damping forces occurs at increasing whirl frequencies due to entrained air in the film flow field. Increasing the lubricant supply pressure reduces the extent of air entrainment and increases damping forces.

This literature review has examined relevant SFD literature published over the past twenty years. Various SFD configurations – open and closed ends, feed grooves and recirculation annulus, and various oil feeding arrangements – are researched and their performance characteristics understood and predicted. However, among the papers reviewed, only Refs.[19- 21] investigate purportedly two parallel SFDs separated by a central feed groove.

CHAPTER III

TEST RIG DESCRIPTION

The test rig is designed to replicate typical operating conditions of a squeeze film damper (SFD) used in jet engines. Test data obtained from conducting measurements on the test rig serve to validate predictions from a companion SFD computational tool [27]. The test rig consists of two electromagnetic shakers, a test rig structure, a static loader, a data acquisition (DAQ) board and computer. Figure 2 shows a picture of the test rig, with the test SFD structure, shakers and static loader firmly mounted on a cast iron table. Figure 3 depicts isometric and top views of the test rig [5]. Table 1 summarizes the test rig components and their function [28]. Table 2 lists the physical dimensions of the squeeze film damper section.

Table 1.SFD test rig components and their function

Component	Quantity	Function
Bearing pedestal	1	Supports entire test structure
Journal base	1	Holds journals A or B
Stationary Journal	2	Journal A: film land length $2L$ Journal B: film land length L
Bearing cartridge	1	Houses sensors for displacement, acceleration and pressure
Main Support rods	4	Support and align bearing cartridge with respect to journal, provide support stiffness
Flexural rods	12	Provide additional support stiffness without affecting alignment
Stinger and static loader attachments	2 + 1	Attachments for shaker stingers and static loader springs to bearing
Seal Ring Installer	1	Assists in insertion of journal into BC with seal rings installed

Table 2. Dimensions of the test dampers

Dimension	Description	Value
c	Nominal radial clearance	127 μm
L	Land length	12.7 mm
D	Journal diameter	0.127 m
c_A	Measured radial clearance of Journal A	141 μm
c_B	Measured radial clearance of Journal B	138 μm

The distinctive features of the test rig are [28]

(a) Two electromagnetic shakers deliver dynamic loads to the bearing cartridge, maximum 2,200N and frequency to 500 Hz. Eddy current displacement sensors measure the relative motions between the bearing and journal.

(b) Two journals, B and A, render squeeze film axial lengths of $L = {}^1\!/_5\,D$ and $2L$ adjacent to a central feed groove. The nominal radial film clearances are c for both journals, while the measured clearances are c_A and c_B; see Table 2. The journals can be easily swapped to change the damper film land lengths.

(c) A modular design of the test rig enables varying the squirrel cage support stiffness by addition and removal of rods. A lubrication system delivers ISO VG 2 grade lubricant oil at room temperature ($T \approx 25^\circ$C) to the test rig at a flow rate up to 47 liter/min.

(d) Sensors measure applied dynamic loads, bearing displacements and accelerations, applied static pull load, lubricant supply pressure and flow rates, static and dynamic pressures in the film lands and central groove, and lubricant temperatures at the inlet and discharge ports.

(e) A Multiple Input Multiple Output (MIMO) automated data acquisition system generates shaker control signals and acquires data from all sensors for post processing in MathCAD®.
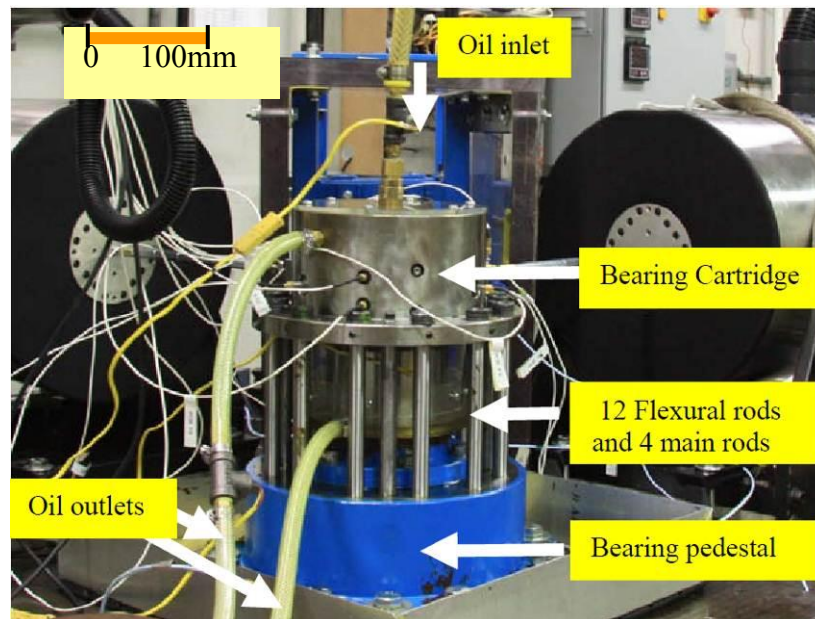
Figure 2. Picture of test rig, shakers and static loader mounted on a cast iron table
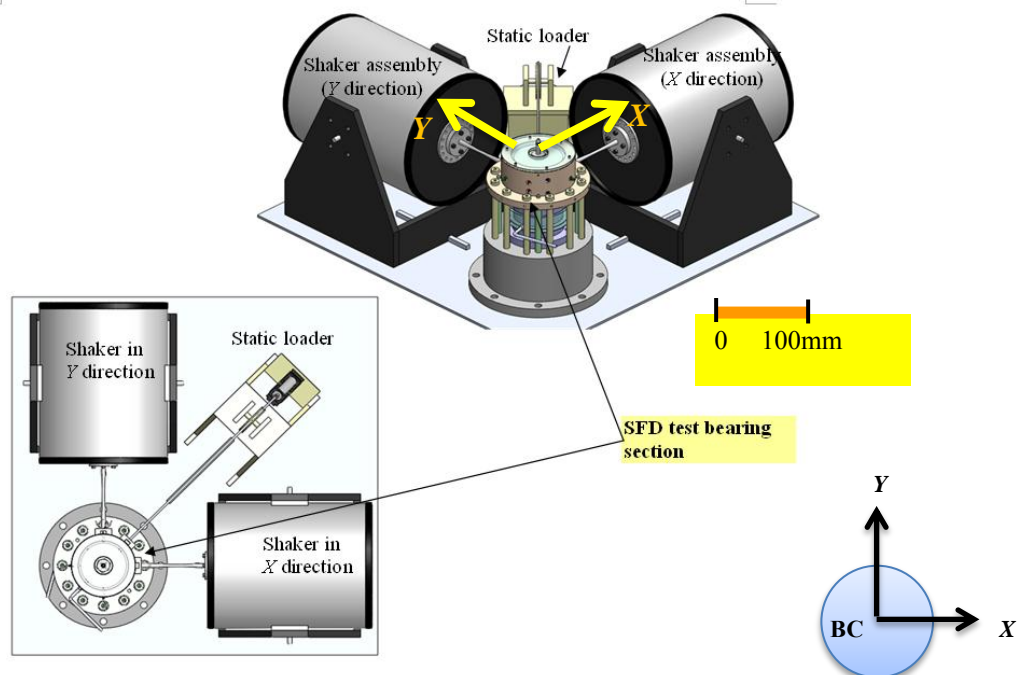
Figure 3. Isometric and top views of test rig. Coordinate system (*X, Y*) shown

Figure 4 shows an exploded view of the test rig and lists individual components and states their function.

The test rig pedestal is mounted atop an oil containment tray and a neoprene mat for vibration isolation. Bolts firmly fasten the pedestal to the cast iron table, and the journal base to the pedestal. A test journal, A or B, fits into the journal base and is secured in place by a cap screw bolt.
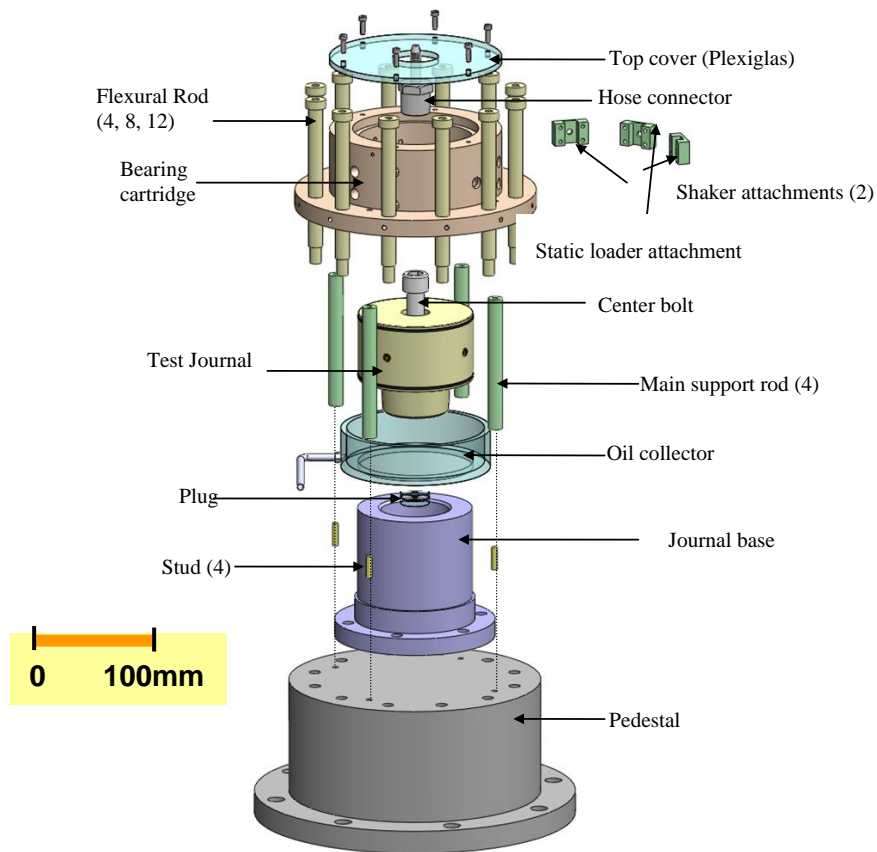
Figure 4. Exploded view of squeeze film damper test rig

The bearing cartridge (BC) is supported on a number of alloy steel rods - 4 non-removable main support rods (MSRs) and up to 12 removable rods. The 4 MSRs align and center the bearing cartridge with respect to the stationary journal and the other rods (0 to 12 in number) provide additional lateral stiffness to the test structure. The flexural rods fit loosely through holes in the BC and are fastened into threaded holes in the pedestal. Studs pin the flexural rods against the BC, hence preventing their relative movement [16]. The BC has a central groove of width L and depth ¾ L, machined at the mid-plane.

The bearing cartridge is accurately aligned and centered with the respect to the journal to obtain a uniform nominal radial clearance (c) around the BC. On assembly, the elastically supported bearing cartridge together with the stationary journal form two parallel squeeze film lands separated by a central groove.

Figure 5 shows front and isometric views of the bearing cartridge (BC). The BC accommodates most sensors as well as attachments to connect to the shakers and to the static loader. The sensors include two eddy current displacement sensors, two piezoelectric accelerometers and six dynamic pressure sensors. In addition, the BC connects to the shaker stingers through piezoelectric load cells and to the static loader springs via a strain-gage type static load cell.
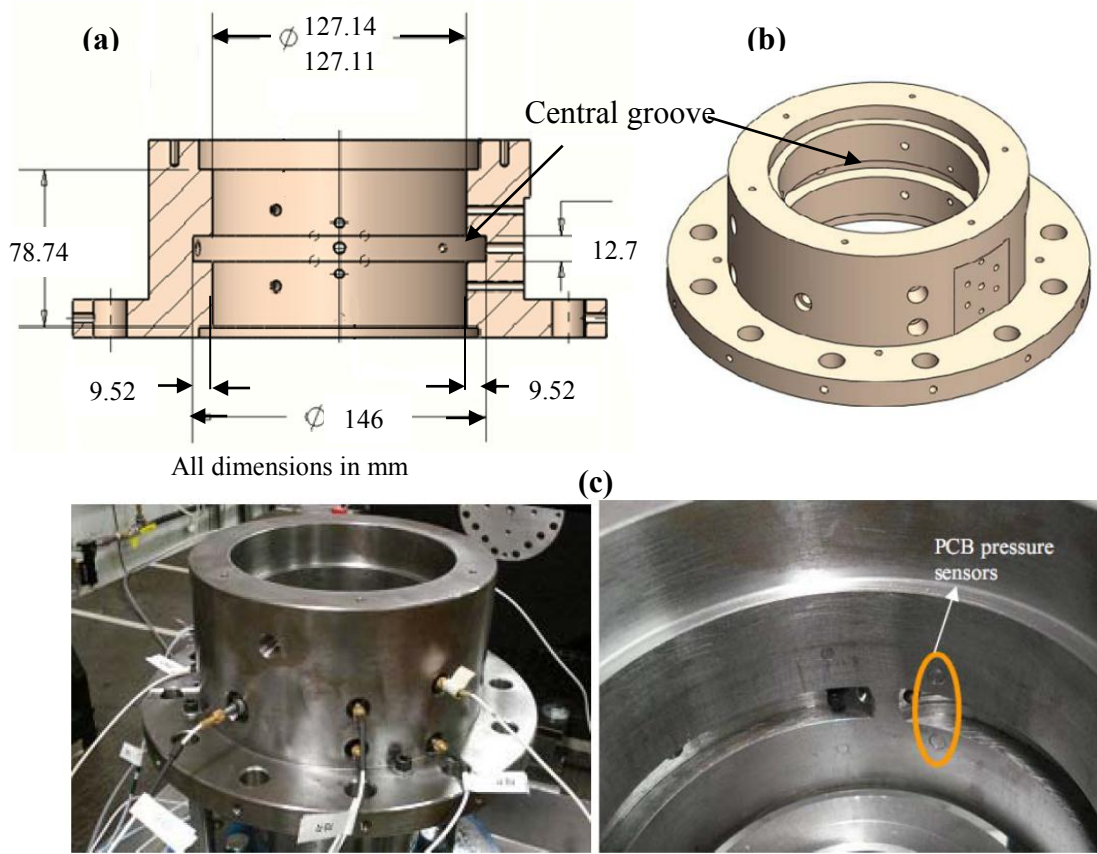
Figure 5. Bearing cartridge (a) cross sectional view (b) front view (c) Photographs showing BC with installed sensors. Taken from [27]

Two test journals A and B can be installed to make parallel dampers with film lengths equaling $2L$ and L respectively. Figures 6 and 7 depict cross sectional and isometric views of journals A and B, respectively. Lubricant oil enters the journals through a central vertical hole and exits into the central groove via three orifice restrictor holes spaced 120° apart, each of 2.54 mm diameter. Grooves machined on the journal ends serve to seat piston ring seals. The two journals, due to small differences in their diameter, determine average radial clearances c_A and c_B. From measurements, $c_A = 1.11c$, $c_B = 1.086c$ ($c_A = 1.022c_B$).
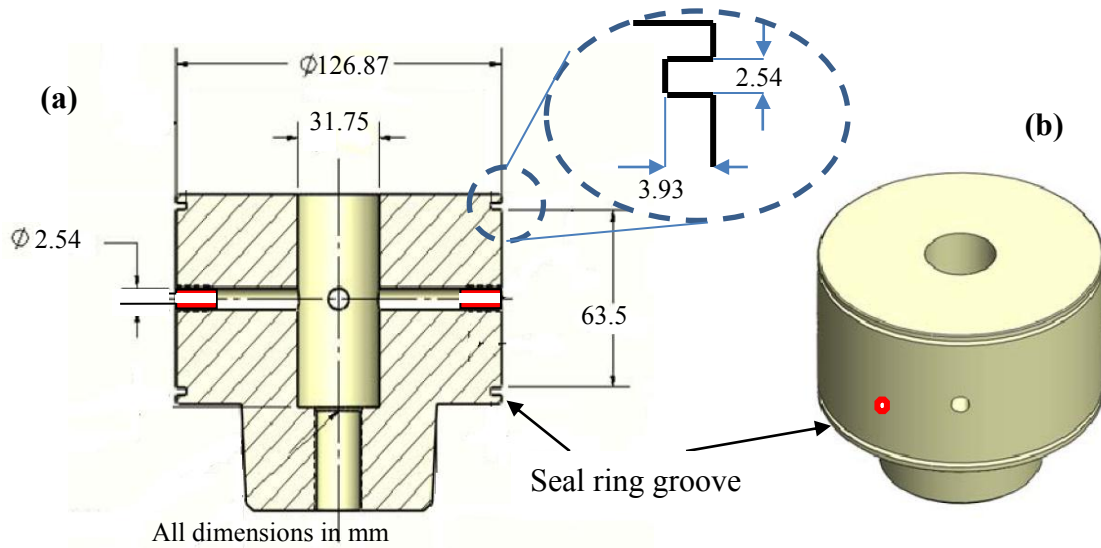
Figure 6. Test Journal A (long journal) (a) cross sectional view (b) Isometric view. Two parallel squeeze film lands of length 2*L* each. Details of piston ring groove shown
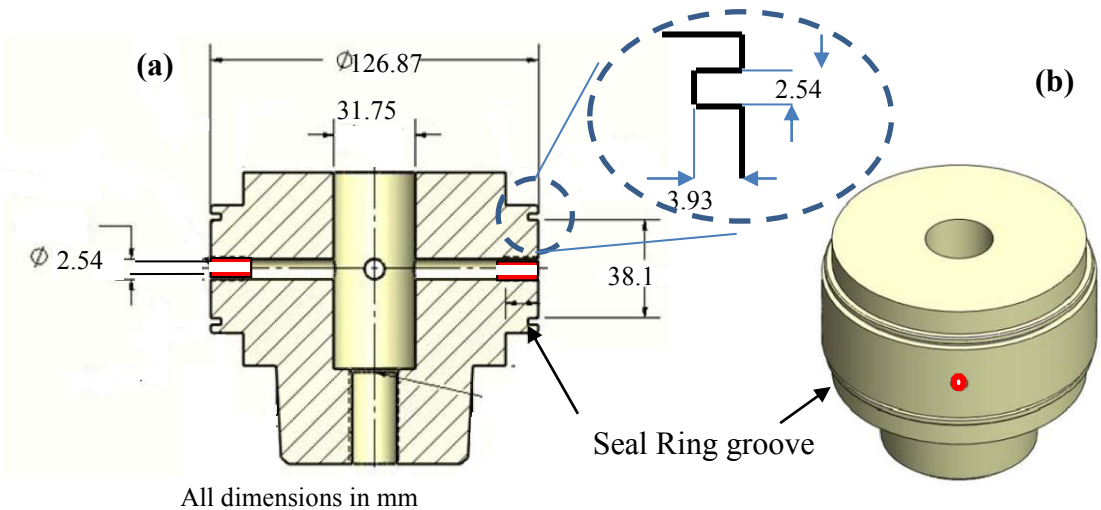
Figure 7. Test Journal B (short journal) (a) cross sectional view (b) Isometric view. Two parallel squeeze film lands of length *L* each. Details of piston ring groove shown

A manually-operated hydraulic cylinder mounted in a sturdy frame comprises the static loader. Two parallel extension springs (140.1 kN/m stiffness) connect the cylinder piston to the test bearing and serve to pull (displace) the BC to a static off-centered

position with respect to the journal. The springs provide structural isolation to the test structure. Two orthogonally positioned electromagnetic shakers excite the elastically supported bearing cartridge with periodic forces by means of slender stingers. The static loader axis is positioned at 45° to the shaker axes.

III. 1 Data acquisition system

A dedicated DAQ system records and displays the signals from various sensors installed in the test rig, and control shaker operation. The recorded test data is processed using MathCAD$^{®}$ worksheets to identify test system force coefficients, namely stiffness, mass and damping.

The DAQ board reads signals from the sensors and generates analog shaker control signals. The board has twenty voltage channels, four thermocouple channels and four analog voltage output channels. A LabVIEW$^{®}$ virtual instrument (VI), modified from a VI developed by Delgado [29], records sensor signals, and generates shaker control signals in real time. The measurement procedure calls for acquisition of various signals at different excitation frequencies while the BC undergoes dynamic motions of constant amplitude over the entire frequency range. The recorded signals include shaker applied loads ($F_{X(t)}$, $F_{Y(t)}$), bearing displacements ($x_{(t)}$, $y_{(t)}$) relative to the stationary journal, bearing accelerations ($a_{X(t)}$, $a_{Y(t)}$), and film land and groove pressures at various locations. Figure 3 defines the test rig axes.

The VI accepts a user-defined vector of frequencies spanning the test range. At each frequency, an iterative motion control algorithm generates voltage control signals for the *X* and *Y* shakers to maintain preset dynamic displacement amplitudes. The VI is capable of generating and controlling rectilinear (unidirectional), circular and elliptical orbits in the test rig. Figure 8 presents a screenshot of the VI showcasing its main features as noted by colored labels.

Figure 8. Screenshot of LabVIEW® Virtual Instrument (VI) main control screen

III.2 Lubricant supply system

Figure 9 depicts a schematic view the test rig lubrication system. A 150 liter storage tank holds lubricant oil at room temperature. A gear pump driven by a 3.5 kW motor delivers oil to the test rig via the journal inlet. Flowmeters installed on the supply and bottom return line measure the inflow rate (Q_{in}) and flow rate exiting the bottom damper (Q_B). Oil exiting the top land collects in the plenum and the flow from bottom land collects in an oil collector tray. A gear pump continuously evacuates the exiting lubricant and pumps it back to the storage tank.
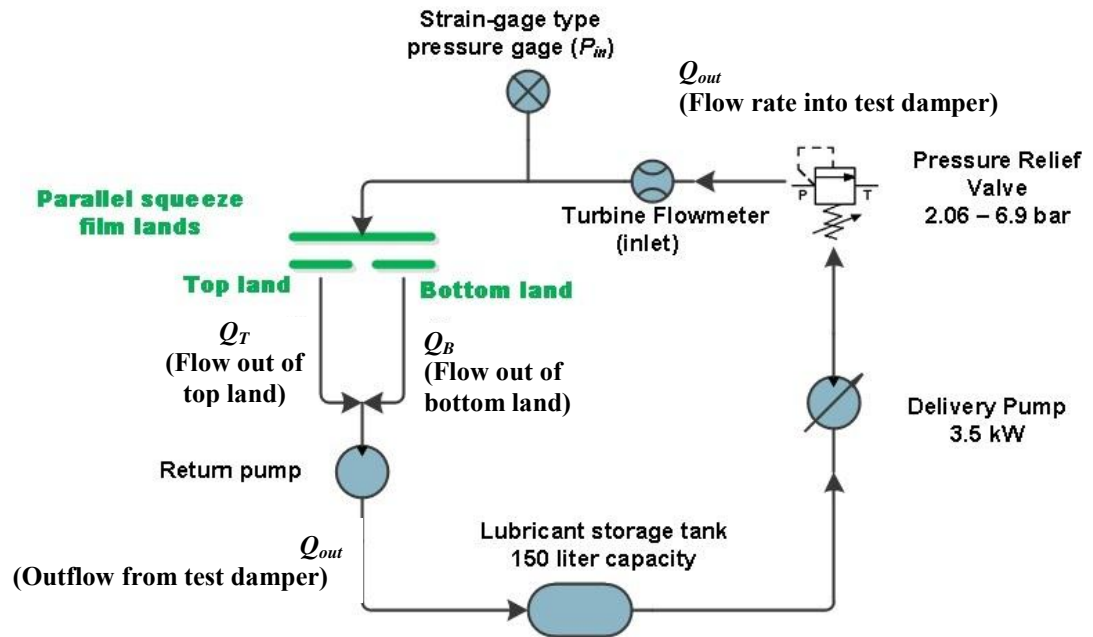
Figure 9. Schematic view of lubrication system

CHAPTER IV

MEASUREMENT OF LUBRICANT VISCOSITY AND FLOW RATES

The lubricant used in the test rig is an ISO VG 2 grade oil. This lubricant replicates at room temperature the viscosity of the actual lubricant operating at high temperature in an aircraft engine. The lubricant density is determined by weighing, at an ambient temperature of $25^{\circ}C$, one liter of oil. The oil density is $\rho = 785 \pm 0.5$ kg/m^3 [30].

A rotary viscometer records to the lubricant viscosity at increasing temperatures, as shown in Figure 10. The viscosity data fit well the equation

$$\mu = \mu_R e^{-\alpha_v(T-T_R)} \tag{1}$$

which is in accordance with the ASTM standard viscosity-temperature for mineral oil lubricants [30].

In the above equation, $(\mu_R, T_R) = (2.96 \text{ x } 10^{-3}$ Pa·s, $25.2^{\circ}C)$ are a reference viscosity and temperature, respectively. The coefficient α_v is obtained from two sets of measured viscosity and temperature as

$$\alpha_v = \frac{\ln(\mu_2/\mu_R)}{(T_2-T_R)} = 0.0187/^{\circ}C \tag{2}$$
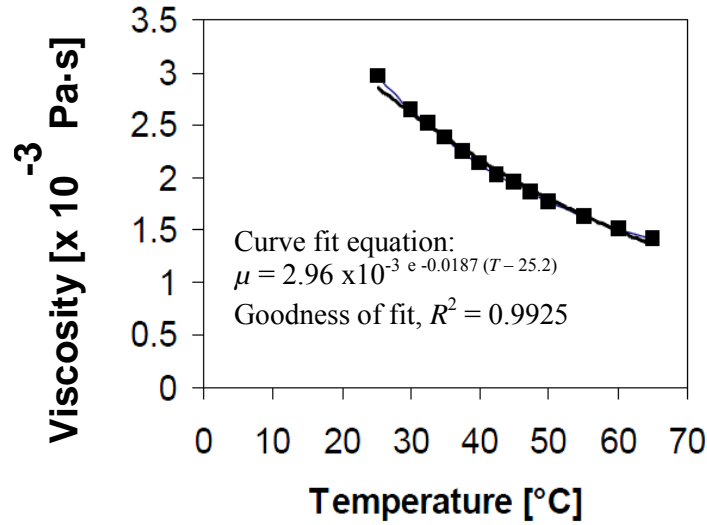
Figure 10. Measured lubricant viscosity versus temperature. Viscosity measured by a rotary viscometer

Since the oil is always at or close to room temperature (25°C), the viscosity is henceforth assumed constant as $\mu = \mu_{25} = 2.96 \times 10^{-3}$ ($\pm 0.005 \times 10^{-3}$) Pa·s. Note that the viscometer measures to an accuracy of 0.01 cP; hence causing a measurement uncertainty of 0.005 cP, equivalent to 0.005×10^{-3} Pa·s.

Flow rate measurements conducted both dampers with a centered bearing cartridge aim to assess the evenness of the flows in the parallel film lands (top and bottom) and to determine their hydraulic resistances [31]. Figure 11 presents a schematic hydraulic circuit diagram of flow through the damper. ISO VG2 oil at $\sim 23^{\circ}$C is pumped through the damper at supply pressure P_{in}. A turbine flowmeter with measurement range 1.14 – 11.36 liters per minute records the flow rate into the damper (Q_{in}). The lubricant enters the central groove with pressure P_G, through three orifice feed holes of resistance R_o. The lubricant then flows through the top and bottom lands with flow rates Q_T and Q_B, respectively. The film land sections have resistances R_T and R_B. The lubricant finally exits to ambient at pressure P_a. The flow rate of lubricant exiting the bottom damper, Q_B, is less than the minimum measurement capability of the installed flowmeter (at least 1.1

liters per minute). The flow rate Q_B is presently measured by recording the time to fill a known volume ($V = 0.17 \pm 0.019$ liters) in the oil collector bucket.
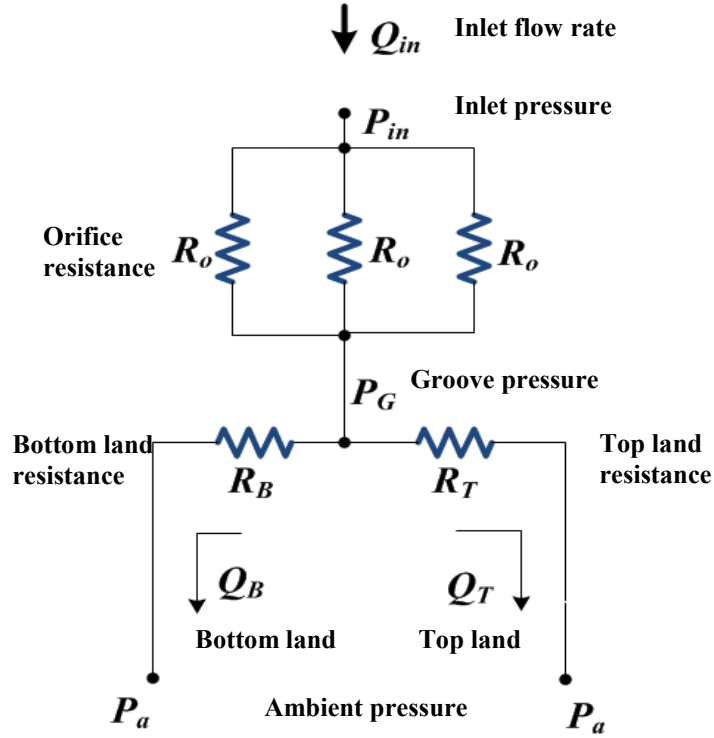
Figure 11. Equivalent hydraulic circuit for open ends (short length and long) dampers

The flow resistance in a squeeze film land relates the lubricant pressure drop across the land to the flow rate through the land. The flow conductances of the film lands (C_T and C_B) are the reciprocals of the flow resistances, i.e.,

$$C_T = \frac{1}{R_T} = \frac{Q_T}{P_G - P_a} \text{ and } C_B = \frac{1}{R_B} = \frac{Q_B}{P_G - P_a} \tag{3}$$

Note that all pressures are gage; hence, $P_a = 0$. Figure 12 shows the measured flow rates (Q_{in}, Q_B) versus groove pressures (P_G). Note the ratio Q_B is nearly 50% of Q_{in} for both dampers, indicating evenness of flow through the top and bottom film lands. Hence, the top film land has nearly the same conductance as the bottom film land ($C_T \approx C_B$).

The slope of a linear curve fit of the flow measurements renders the bottom land flow conductances; C_B = 4.60 ±0.35 LPM/bar for the long damper and C_B= 8.88 ±0.55 LPM/bar for the short length damper. The short length damper has twice the flow conductance of the long damper since the shorter land lengths offer lesser resistance to the lubricant flow. Note that the measurements were conducted twice and giving similar results.
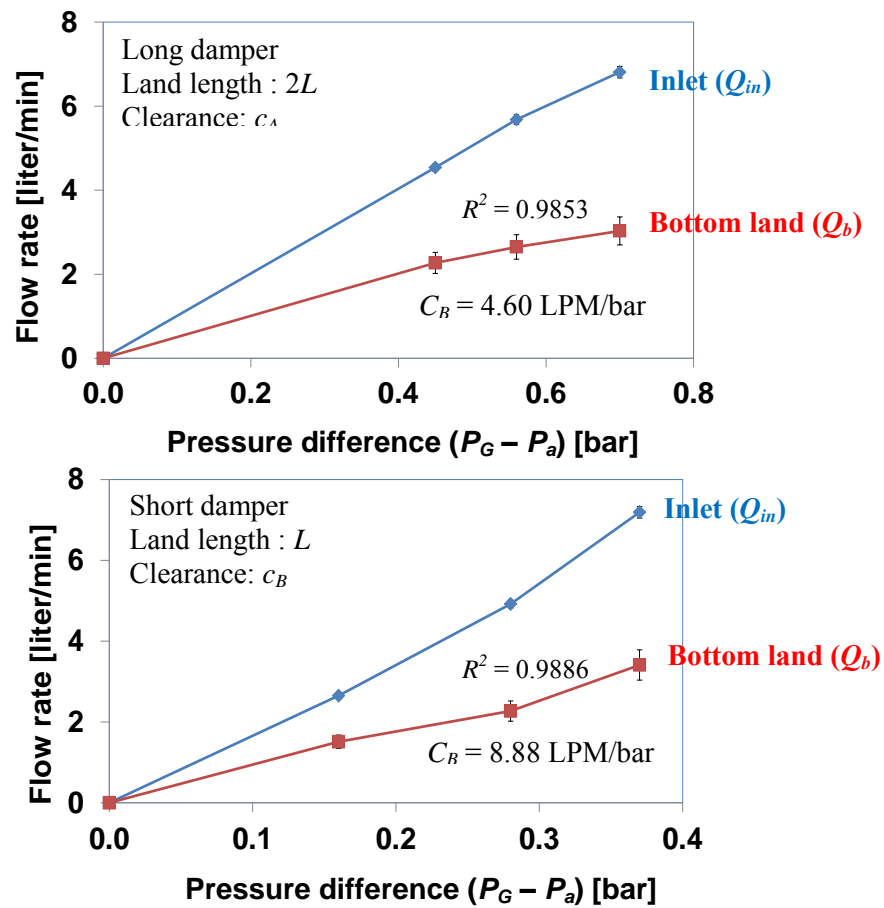
Figure 12. Flow rates versus pressure difference for long (top) and short length (bottom) open ends dampers

The flowmeter manufacturer specifies a flow rate measurement uncertainty ($U_{Q_{in}}$) as 2% and a repeatability of ±0.1%.

Recall that Q_B is calculated by recording the time taken (t) to fill a known volume V = 0.17 ±0.019 liters in the oil collector bucket, i.e., $Q_B = V/t$. The uncertainty in the measurement of the time t is U_t= 0.05s. The uncertainty (U_{Q_B}) in the measurement of the bottom flow rate ($Q_B = V/t$), using the Kline-McClintock procedure [32] is 11%.

Uncertainties in conductances for the short length and long dampers are obtained as

$$U_C = 0.5 \text{ x } (C_{High} - C_{low}) \tag{4}$$

where C_{High} and C_{low} are the largest and smallest slopes (conductances) obtained from drawing linear trend lines through the data points in Figure 12.

CHAPTER V

IDENTIFICATION OF SFD DAMPING AND ADDED MASS
COEFFICIENTS

The current chapter is based on the mid-year technical progress report delivered to the project sponsor [33]. The BC is aligned and centered with respect to the rigid journal (A or B) before commencement of a series of tests for each SFD configuration. Impact load tests and unidirectional load tests on the dry (unlubricated) system serve to identify dry system force coefficients viz., structural stiffness $(\mathbf{K_S})$, mass $(\mathbf{M_S})$, and remnant damping $(\mathbf{C_s})$. Similarly, circular and elliptical orbit tests on the lubricated system serve to identify lubricated system mechanical parameters ($\mathbf{K}$, $\mathbf{C}$, $\mathbf{M}$). A computational worksheet processes the acquired dynamic load and displacement signals and utilizes the ensuing identification procedure [9] to identify dry or lubricated system parameters. Subtraction of dry parameters from lubricated system parameters gives the mechanical parameters of the squeeze film alone ($\mathbf{K_{SFD}}$, $\mathbf{C_{SFD}}$, $\mathbf{M_{SFD}}$).

Two variations of the identification procedure are used; one for a stationary and rigid journal (short length damper), and another for a moving journal (long damper).

Figure 13 schematically depicts the structural and squeeze film force coefficients.
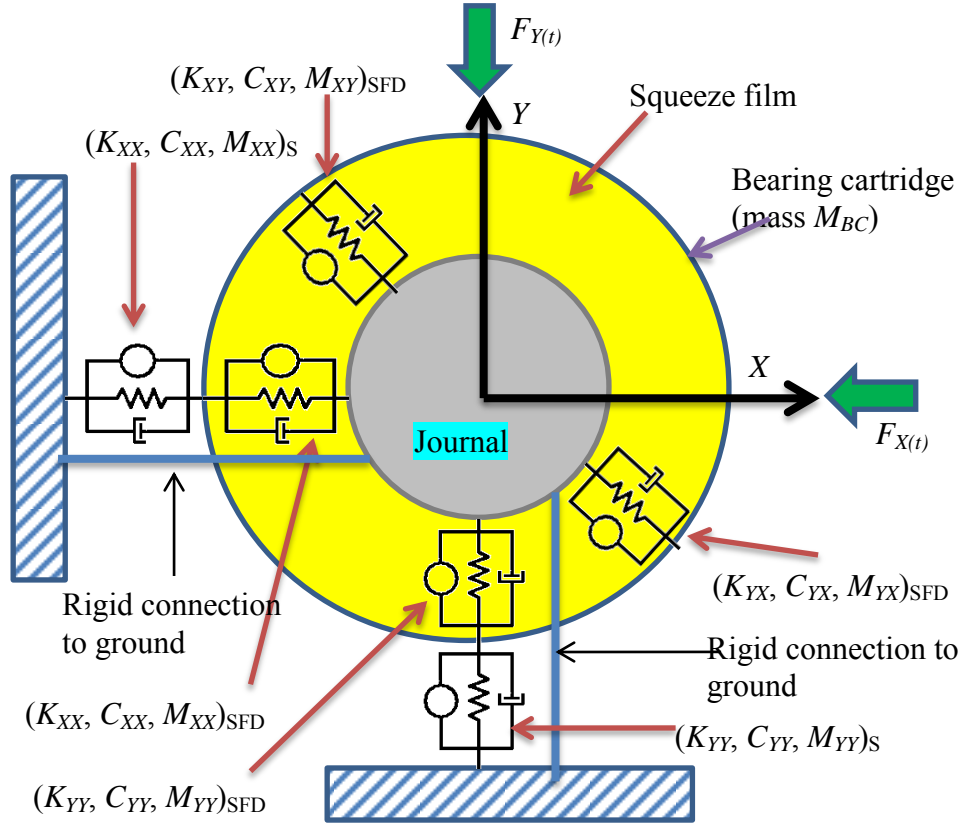
Figure 13. Schematic representation of force coefficients of the structure and the squeeze film. Modified from [9]

For both the dampers, impact load tests consist of exciting the (dry) structure with a series of manually-delivered impacts $F_{X(t)}$ and $F_{Y(t)}$ using a calibrated impact hammer, along the X and Y axes of the test rig. In case of unidirectional tests, the shakers deliver single frequency loads, k in number; $F_{X(t)}$ along X direction (Y shaker off) and $F_{Y(t)}$ along the Y direction (X shaker off). The load vectors for impact load and unidirectional load tests are written as

$$\mathbf{F_1} = \begin{bmatrix} F_{X(t)} \\ 0 \end{bmatrix} \text{ and } \mathbf{F_2} = \begin{bmatrix} 0 \\ F_{Y(t)} \end{bmatrix} \tag{5}$$

In case of circular and elliptical orbit tests, shakers impose single frequency loads on the BC along X and Y directions to maintain specified orbit shapes. The phase difference

between the load signals is set approximately $+90^\circ$ and -90°, to induce clockwise and anticlockwise whirl orbits. The data acquisition code adjusts the load amplitude to maintain a preset orbit size at each excitation frequency.

The independent single frequency load vectors in the time domain are [30]

$$\mathbf{F_1} = \begin{bmatrix} F_{X_1} \cos(\omega t) \\ -F_{Y_1} \sin(\omega t) \end{bmatrix} = \text{Re}\left(\begin{bmatrix} F_{X_1} \\ iF_{Y_1} \end{bmatrix} e^{i\omega t} \right)$$

$$\mathbf{F_2} = \begin{bmatrix} F_{X_2} \cos(\omega t) \\ F_{Y_2} \sin(\omega t) \end{bmatrix} = \text{Re}\left(\begin{bmatrix} F_{X_2} \\ -iF_{Y_2} \end{bmatrix} e^{i\omega t} \right) \tag{6}$$

V.1 Short length damper

The equations of motion for the test system supplied with lubricant and excited by external shaker forces are [33]

$$\mathbf{M_s}\ddot{\mathbf{z}} + \mathbf{C_s}\dot{\mathbf{z}} + \mathbf{K_s}\mathbf{z} = \mathbf{F_{(t)}} + \mathbf{F_{SFD}} \tag{7}$$

For the short length damper, the journal is taken as stationary (non-moving); hence, the accelerations (**a**) are derived from measured BC displacements relative to the stationary journal.[1]

In the above equation, $\mathbf{z} = (\,x_{(t)},\,y_{(t)}\,)^{\text{T}}$ is the vector of ensuing BC displacements, ($\mathbf{K_s}$, $\mathbf{C_s}$, $\mathbf{M_s}$) are the dry system mass, damping and stiffness matrices, $\mathbf{F_{(t)}}$ is the shaker forces vector, and $\mathbf{F_{SFD}}$ is the vector of SFD reaction forces. The SFD reaction forces, i.e., the forces generated in the lubricant film in response to an external forced excitation, are modeled as

$$\mathbf{F_{SFD}} = -\mathbf{M_{SFD}}\ddot{\mathbf{z}} - \mathbf{C_{SFD}}\dot{\mathbf{z}} - \mathbf{K_{SFD}}\mathbf{z} \tag{8}$$

where ($\mathbf{M_{SFD}}$, $\mathbf{C_{SFD}}$, $\mathbf{K_{SFD}}$) represent the mechanical parameters of the squeeze film. Substitution of Eq.(8) into Eq.(7) gives

$$\mathbf{M}\ddot{\mathbf{z}} + \mathbf{C}\dot{\mathbf{z}} + \mathbf{K}\mathbf{z} = \mathbf{F_{(t)}} \tag{9}$$

---

[1] At each test frequency ω, the measured accelerations **a** are harmonic, i.e., $\mathbf{a} = -\omega^2\mathbf{z}.$

In the above equation, $\mathbf{M}=\mathbf{M_s} + \mathbf{M_{SFD}}$, $\mathbf{C}=\mathbf{C_S} + \mathbf{C_{SFD}}$ and $\mathbf{K}=\mathbf{K_s} + \mathbf{K_{SFD}}$

Eqn.(9), when transformed into the frequency domain, becomes

$$[\mathbf{K} \text{-} \mathbf{M}\omega^2 + i\omega\mathbf{C}]\, \overline{\mathbf{z}}_{(\omega)} = \overline{\overline{\mathbf{F}}}_{(\omega)} \tag{10}$$

where $\overline{\mathbf{z}}_{(\omega)} = \{\overline{\mathbf{z}}_{1(\omega)}, \overline{\mathbf{z}}_{2(\omega)}\}^T$ and $\overline{\mathbf{F}}_{(\omega)} = \{\overline{\mathbf{F}}_{1(\omega)}, \overline{\mathbf{F}}_{2(\omega)}\}^T$ are the Fourier transforms of $\mathbf{z}_{(t)}$ and $\mathbf{F}_{(t)}$ respectively. On defining the system impedance matrix $\mathbf{H}$ as

$$\mathbf{H}_{(\omega)} = [\mathbf{K} \text{-} \mathbf{M}\omega^2 + i\omega\mathbf{C}] \tag{11}$$

Eq.(11) becomes

$$\mathbf{H}_{(\omega)}\, \overline{\mathbf{z}}_{(\omega)} = \overline{\overline{\mathbf{F}}}_{(\omega)} \tag{12}$$

Recall that two independent load vectors excite the test system to result in linearly independent displacements [9]. Eq.(13) finds the components of the impedance matrix $\mathbf{H}_{(\omega)}$

$$\mathbf{H}_{(\omega)} = \begin{bmatrix} H_{XX} & H_{XY} \\ H_{YX} & H_{YY} \end{bmatrix} = \begin{bmatrix} \overline{\mathbf{F}}_1 & \overline{\mathbf{F}}_2 \end{bmatrix} \begin{bmatrix} \overline{\mathbf{z}}_1 & \overline{\mathbf{z}}_2 \end{bmatrix}^{-1} \tag{13}$$

The flexibility matrix $\mathbf{G}$ is determined by inverting the impedance matrix $\mathbf{H}$. That is

$$\mathbf{G} = \mathbf{H}^{\text{-}1} \tag{14}$$

Stacking the real and imaginary parts of measured flexibility functions at each test frequency ω_k results in a matrix $\mathbf{A}$. The least square method uses the matrix $\mathbf{A}$ to determine initial estimates of the lubricated system force coefficients ($\mathbf{K, C, M}$) [9].

$$\begin{bmatrix} \underline{\mathbf{M}} \\ \underline{\mathbf{C}} \\ \mathbf{K} \end{bmatrix} = (\mathbf{A}^T\mathbf{A})^{-1}\mathbf{A}^T\mathbf{I} \tag{15}$$

The Instrumental Variable Filter (IVF) method uses a similar procedure as in Eq.(15), but it is iterative in nature. A new weighting function $\mathbf{W}^{(m)}$ is built from the identified force coefficients from the previous iteration $\mathbf{W}^{(m\text{-}1)}$, where m is the iteration index. Note that $\mathbf{W} =\mathbf{A}$ for the first iteration (m=1), corresponding to the least squares solution. The force coefficients in each subsequent ($m \geq 2$) iteration are given by

$$\begin{bmatrix} \mathbf{M} \\ \hline \mathbf{C} \\ \hline \mathbf{K} \end{bmatrix}^{m} = ([\mathbf{W}^{(m-1)}]^{\mathbf{T}}\mathbf{A})^{-1}[\mathbf{W}^{(m-1)}]^{\mathbf{T}}\mathbf{I} \tag{16}$$

The iterative process continues until a predefined tolerance level between two consecutive estimations is attained, yielding test system coefficients influenced minimally by measurement errors [9].

The SFD force coefficients follow by subtracting the dry system parameters from the identified lubricated system parameters. That is,

$$(\mathbf{K, C, M})_{\mathbf{SFD}} = (\mathbf{K, C, M}) - (\mathbf{K, C, M})_{\mathbf{S}} \tag{17}$$

V.2 Long damper

For the long damper, the BC accelerations are derived directly from accelerometer measurements. The equation of motion of the dry (unlubricated) system is

$$M_{BC}\mathbf{a} + \mathbf{M}_{\mathbf{rs}}\ddot{\mathbf{z}} + \mathbf{C}_{\mathbf{s}}\dot{\mathbf{z}} + \mathbf{K}_{\mathbf{s}}\mathbf{z} = \mathbf{F}_{(t)} \tag{18}$$

where $\mathbf{a} = (a_{X(t)}, a_{Y(t)})^{\mathrm{T}}$ is the vector of measured BC accelerations, M_{BC} is the effective BC mass[2], $(\mathbf{K_S, C_S, M_{rS}})$ are the stiffness, remnant damping and residual mass matrices of the dry structure. Note here that $\mathbf{z}$ is the vector of displacements of the BC relative to the journal base.

On transformation to the frequency domain, Eq. (18) becomes

$$[\mathbf{K_S} - \mathbf{M_{rS}}\omega^2 + i\omega\mathbf{C_S}]\,\overline{\mathbf{z}}_{(\omega)} = \overline{\overline{\mathbf{F}}}_{\mathbf{e}(\omega)} \tag{19}$$

where $\overline{\overline{\mathbf{F}}}_{\mathbf{e}(\omega)} = \overline{\mathbf{F}}_{(\omega)} - M_{BC}\overline{\mathbf{a}}_{(\omega)}$, $\overline{\mathbf{a}}_{(\omega)} = DFT(\mathbf{a})$.

On defining the dry system impedance matrix as $\mathbf{H_{dry}} = (\mathbf{K_S} - \mathbf{M_{rS}}\omega^2 + i\omega\mathbf{C_S})$, Eq.(19) becomes

$$\mathbf{H_{dry}}\,\overline{\mathbf{z}}_{(\omega)} = \overline{\overline{\mathbf{F}}}_{\mathbf{e}(\omega)} \tag{20}$$

---

[2] The sixteen rods behave as cantilever beams and contribute 1/4 of their mass to the BC mass. Hence, the effective BC mass M_{BC} adds the measured mass of the instrumented BC and ¼ the total mass of the rods

and the dry system flexibility function is

$$\mathbf{G_{dry}} = \mathbf{H_{dry}^{-1}}$$
(21)

The IVFM curve fits the dry system flexibility function $\mathbf{G_{dry}}$ to estimate the parameters ($\mathbf{K_S}$, $\mathbf{C_S}$, $\mathbf{M_{rS}}$) . Note that $\mathbf{M_{rS}}$ is a residual mass matrix whose elements are of small magnitude.

For a lubricated test system, the equations of motion are

$$M_{BC}\mathbf{a} + \mathbf{M\ddot{z}} + \mathbf{C\dot{z}} + \mathbf{Kz} = \mathbf{F_{(t)}}$$
(22)

where $\mathbf{M} \approx \mathbf{M_{rS}} + \mathbf{M_{SFD}}$, $\mathbf{C} = \mathbf{C_S} + \mathbf{C_{SFD}}$, $\mathbf{K} = \mathbf{K_S} + \mathbf{K_{SFD}}$. On transforming Eq.(22) to the frequency domain,

$$[\mathbf{K} - \mathbf{M}\omega^2 + i\omega\mathbf{C}]\, \mathbf{\bar{z}_{(\omega)}} = \mathbf{\bar{F}_{e(\omega)}}$$
(23)

where the lubricated system impedance function is $\mathbf{H} = (\mathbf{K} - \mathbf{M}\omega^2 + i\omega\mathbf{C})$.

The lubricated system flexibility function is $\mathbf{G} = \mathbf{H^{-1}}$. The IVFM curve fits the flexibility function $\mathbf{G}$ to yield the lubricated system mechanical parameters ($\mathbf{K}$, $\mathbf{C}$, $\mathbf{M}$). Finally, the SFD force coefficients are determined from

$$(\mathbf{K, C, M})_{SFD} = (\mathbf{K, C, M}) - (\mathbf{K, C, M})_{rS}$$
(24)

CHAPTER VI

IDENTIFICATION OF TEST STRUCTURE PARAMETERS

The test structure, free of oil, is subjected to impact load or single frequency periodic shaker load tests along the X and Y directions. The identification procedure, following the procedure described in section IV, identifies the test system structural stiffness $(K_S)_{X,Y}$, remnant damping $(C_S)_{X,Y}$ and system effective mass $(M_S)_{X,Y}$. The identified structural force coefficients are termed as 'baseline' parameters.

VI.1 Force coefficients for the structure holding the short length damper

The structure for the short length damper, denoted as structure B, consists of the BC supported on sixteen rods, each rod of diameter 15.88 mm. A static pull test consists of the static loader pulling the BC to various off-centered positions. At each position, a strain-gage type load cell records the pull force and displacement sensors record the ensuing static BC displacements along the X and Y axes. The slope of a resulting displacement-force curve gives the static stiffness of the structure as $K_S^{static} = 6.13 \pm 0.09$ MN/m [33].

Impact load tests on the dry structure serve to identify the dry system parameters $(\mathbf{K}, \mathbf{C}, \mathbf{M})_S{}^{3}$, and consist of delivering a series of impacts on the BC using a calibrated impact hammer and recording the impact force $F_{j,(j=X,Y)}$ and the ensuing displacements $X_{i,(i=X,Y)}$ of the BC with respect to the stationary journal.

Figure 14 shows the experimentally determined flexibility function $G_{ij} = dX_i/dF_j,_{(i,j=X,}$ $_{Y)}$ for the dry system from impact tests, and the corresponding IVF model curve fits. The top graph shows flexibility functions G_{XX} and G_{XY}, and the bottom graph shows G_{YY} and

---

[3] The structural parameters correspond to <u>IVFM-identified</u> structural stiffness ($\mathbf{K_S}$), remnant damping ($\mathbf{C_S}$) and the effective mass ($\mathbf{M_S}$) that includes the BC mass and the mass contribution from the rods.

G_{YX}. The frequency range of parameter identification is 5-150 Hz, which encloses the system natural frequency $f_n = {\sim}90$ Hz.

Table 3 lists the IVFM identified structural parameters along the principal axes [33], and Appendix B lists the corresponding uncertainties. As expected, cross-coupled force coefficients are a negligibly small fraction of the direct coefficients and hence not listed in the table.

The identified direct stiffnesses ($K_{S_{XX}}$, $K_{S_{YY}}$) are within 7% of the static stiffness K_S^{static}. Note that $K_{S_{XX}}$ and $K_{S_{YY}}$ differ by 8%, thus denoting a structural orthotropy. The orthotropy results in a ${\sim}5$ Hz difference between the natural frequencies along X and Y directions. The sharp peaks in the flexibility functions evidence a very low damping ratio $\zeta_S \approx 0.05$. Such low damping ratios are typical of steel structures [30].

The measured mass of the bearing cartridge alone is 16.37 ± 0.002 kg. However, the identified mass coefficients $M_{S_{XX}}$ and $M_{S_{YY}}$ are slightly larger since the sixteen cantilevered support rods contribute 25% of their own mass (1.1 kg) to the BC mass [30]. With the rod contribution included, the effective BC mass is $M_{BC}^{eff} = 17.47$ kg, hence in agreement with the identified parameters listed in Table 3.

(a)

(b)
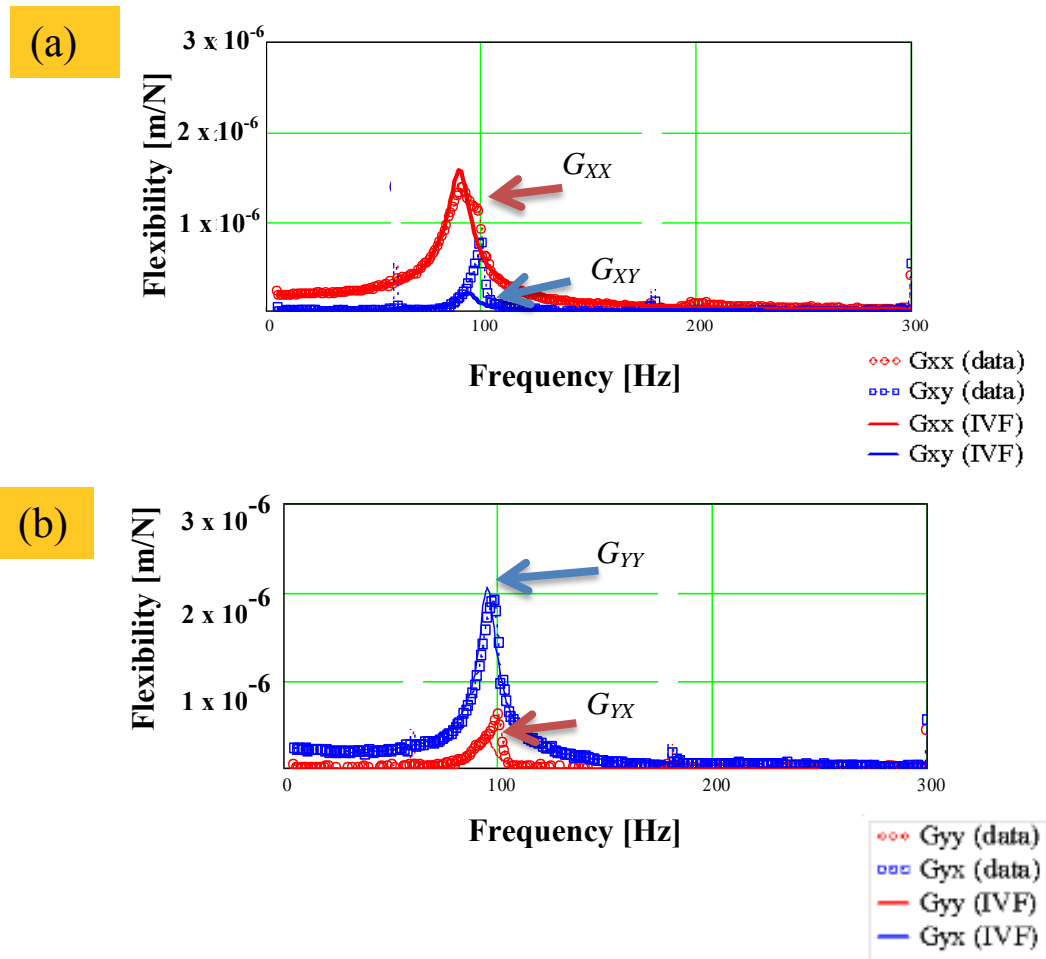
Figure 14. Typical flexibility functions for the <u>dry</u> short length damper support structure, obtained from impact load tests (a) G_{XX} and G_{XY} (b) G_{YY} and G_{YX}. Experimental values and IVF curve fits

Table 3. Dry structure direct parameters for the support structure holding the short length damper . Frequency identification range 5-150 Hz

Direct identified structural parameters	Support structure holding the short length damper	
	X axis	Y axis
Stiffness (K_S) [MN/m]	5.71	6.22
Mass (M_S)* [kg]	17.78	17.37
Damping (C_S) [kNs/m]	1.14	0.82
Natural frequency (f_n) Hz	90.3	95.3
Damping ratio (ξ_s)	0.06	0.04
Static parameters	$K_S^{static} = 6.13 \pm 0.09$ MN/m $M_{BC}^{eff} = 17.5 \pm 0.002$ kg	

*includes BC effective mass

VI.2 Force coefficients for the structure holding the long damper

The structure for the long damper consists of the BC supported on sixteen rods; each of the rods has a diameter of 22.33 mm, i.e., 40% thicker than those of the rods in the structure supporting the short length damper. Thicker rods are installed to increase the support structure stiffness, as instructed by the sponsor. A static pull test gives a structural support stiffness of K_S^{static} =26.27 ± 0.15 MN/m [33], making the structure 4.28 times stiffer than the structure supporting the short length damper.

Single frequency unidirectional load tests on the dry structure serve to identify the dry system parameters (**K**, **C**, **M$_r$**)$_S$ [4]. The electromagnetic shakers deliver single frequency sinusoidal loads on the BC, along one direction at a time. The recorded loads $F_{i,(i=X,Y)}$ and BC displacements $X_{j,(j=X,Y)}$ are used to build flexibility functions $G_{ij} = dX_i/dF_j$, $_{(i,j=X,\ Y)}$. The IVF method curve fits the functions over a frequency range to identify the structural parameters. The frequency range of curve fit, 110-250 Hz, encompasses the system natural frequency $f_n \approx 185$ Hz.

Recall that the identification procedure for the long damper mechanical parameters (both structural and lubricated) uses the measured BC accelerations.

Figure 15 shows the experimental flexibility functions (G_{XX}, G_{XY}) and (G_{YY}, G_{YX}), and their IVFM curve fits. Unlike for the short length damper, the flexibility functions for the long damper do not include the BC mass matrix (M_{BC}). Table 4 lists the IVFM identified structural parameters along the X and Y directions [33].

---

[4] The structural parameters correspond to <u>IVFM-identified</u> structural stiffness (**K$_S$**), remnant damping (**C$_S$**) and the residual mass (**M$_{rS}$**).
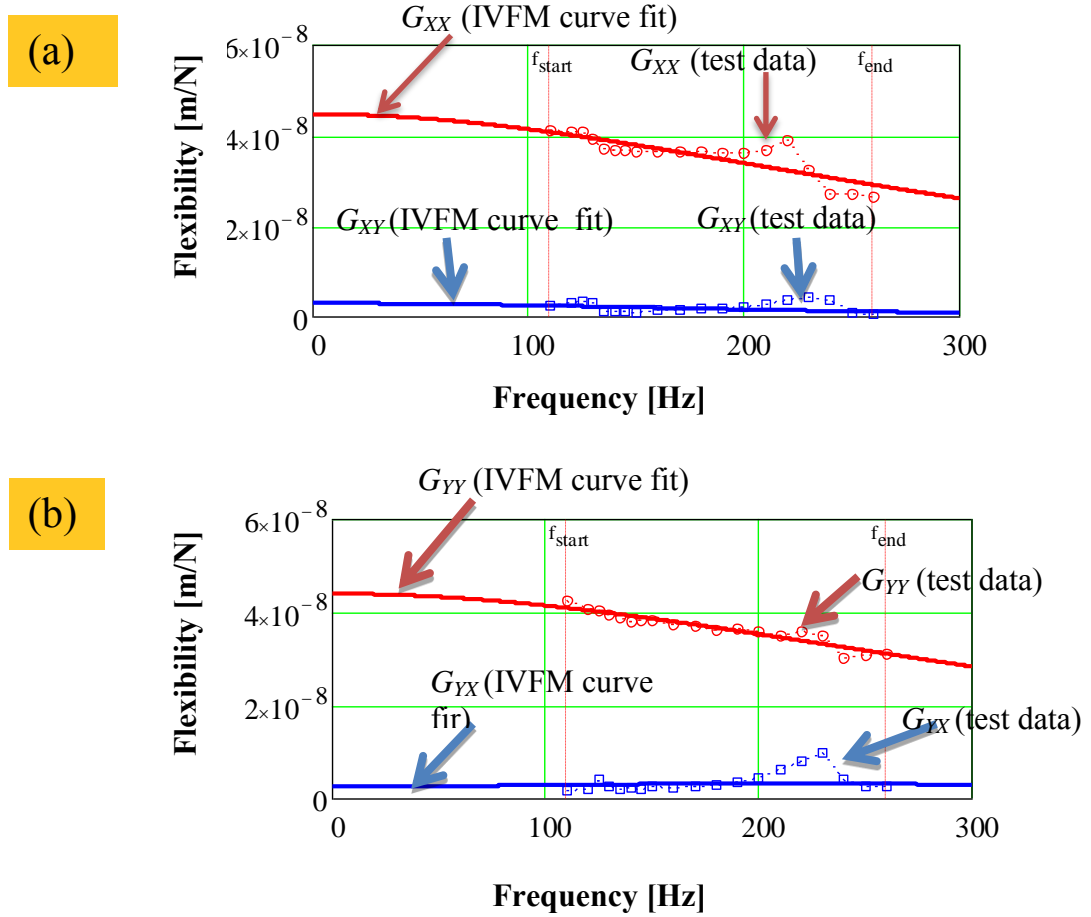
Figure 15. Typical flexibility functions of the <u>dry</u> long damper support structure, obtained from unidirectional load tests of amplitude 0.1c_A (a) G_{XX} and G_{XY} (b) G_{YY} and G_{YX}. Experimental values and IVF curve fits

Table 4 lists the IVFM-identified parameters for the long damper structure and Appendix B lists the uncertainties. Since the frequency identification range excludes very low frequencies (near-static condition), the identified structural stiffnesses $K_{S_{XX}}$ and $K_{S_{YY}}$ differ from the static stiffness K_S^{static} (determined from a static pull test) by ~15%.

In general, only the SFD damping and added mass coefficients are parameters of primary importance. The structural stiffness, if extremely large, arrests the amplitude of

motion and overwhelms the effects of damping. For the current system, the magnitude of stiffness is still low enough to prevent adverse effects on SFD damping performance. Hence an accurate estimation of the stiffness coefficients is not necessary.

Note that the effective BC mass (BC mass and mass contributed by the rods) is 19.44 kg. However, the best goodness of curve fit for the real and imaginary parts of the impedance function is obtained when a BC mass M_{BC} = 22.43 kg, obtained by trial and error, is enforced in the identification procedure. On enforcing M_{BC} = 22.43 kg, the IVF curve fit identifies an residual masses $(M_{rS})_{XX,YY}$ of low magnitudes (See section V.2).

Note that the residual mass matrix M_{rS} does not influence the test rig natural frequencies listed in Table 4. Eq.(25) lists the relations used to determine the natural frequencies f_n and the damping ratios (ξ_s). The low damping ratios $(\xi_s \approx 0.03\text{-}0.06)$ are typical of steel structures.

$$f_n = \frac{1}{2\pi}\sqrt{\frac{K_S^{static}}{M_{BC}^{eff}}} = 185 \text{ Hz} \tag{25}$$

$$\xi_S = \frac{C_S}{2M_{BC}^{eff}\omega_n} = 0.03 \text{ to } 0.06$$

.

Table 4. Dry structure direct parameters for the support structure holding the long damper. Frequency identification range 110-250 Hz. M_{BC} used in IVFM = 22.43 kg

Direct identified structural parameters	Support structure holding the long damper	
	X axis	Y axis
Stiffness (K_S) [MN/m]	22.42	22.8
Residual Mass (M_{rS}) [kg]	- 4.31	- 3.45
Damping (C_S) [kNs/m]	3.1	1.5
Natural frequency (f_n) Hz	185	185
Damping ratio (ξ_s)	0.06	0.03
Static parameters	$K_S^{static} = 26.27 \pm 0.15$ MN/m $M_{BC}^{eff} = 19.440 \pm 0.002$ kg	

CHAPTER VII

FORCE COEFFICIENTS FROM CLASSICAL SFD LUBRICATION
THEORY AND NON-DIMENSIONALIZATION OF SFD
PARAMETERS

Recall that the current test dampers, short and long, consist of two film lands separated by a central groove. Predictive formulas for SFD damping and added mass coefficients based on classical lubrication analysis consider the central groove as a source of lubricant at constant pressure and effectively separating the film lands. In other words, a central groove does not influence the SFD forced performance[5].

For an open ends and centered damper, normalizing direct damping (C^*) and inertia (M^*) coefficients are [34]

$$C^* = 2 \text{ x } 12\pi\mu L \left(\frac{R}{c}\right)^3 \left[1 - \frac{\tanh\left[\frac{L}{D}\right]}{\frac{L}{D}}\right] = C_{XX}^* = C_{YY}^* \qquad (26)$$

$$M^* = 2 \text{ x } \frac{\pi\rho L R^3}{c} \left[1 - \frac{\tanh\left[\frac{L}{D}\right]}{\frac{L}{D}}\right] = M_{XX}^* = M_{YY}^*$$

Note that the lubricant in a SFD does not cavitate for small amplitude journal motions [1]. The relationships above are valid for a full film condition and infinitesimally small amplitude journal motions.

The factor two in the equation above accounts for the two film lands adjacent to the groove. The parameters (μ, ρ) denote the lubricant viscosity and lubricant density and (D, $R=D/2$, L, c) denote journal diameter, journal radius, land length and radial clearance, respectively. The appropriate film length (L) and radial clearance (c) for each SFD test configuration are used to predict the normalizing force coefficients listed in

---

[5] In reality, the central groove in the current test rig affects significantly the overall forced response of lubricated mechanical components, as will be shown later.

Table 5. These coefficients are used to normalize the experimentally identified force coefficients, i.e., $\bar{C} = C/C^*$ and $\bar{M} = M/M^*$

Table 5. Predicted normalizing force coefficients for two parallel film lands separated by a central groove

Long damper	C_A^* (kN-s/m)	M_A^* (kg)
Land length 2L, clearance c_A	6.798	2.985
Short damper	C_B^* (kN-s/m)	M_B^* (kg)
Land length L, clearance c_B	0.918	0.386

CHAPTER VIII

SAMPLE MEASUREMENTS OF DYNAMIC PRESSURE IN THE FILM LANDS AND GROOVE FOR THE LONG DAMPER

Six piezoelectric pressure sensors installed in the BC serve to measure the dynamic fluid pressure fields at mid-axial length of the squeeze film lands and in the central groove. Two pressure sensors, installed 120° apart, record the dynamic pressures in the top squeeze film land, and a similar setup of sensors measures pressure fields in the bottom film land. Two other sensors in the central groove measure the groove pressures. The sensor disposition changes with the damper land lengths, long and short. Figure 16 depicts the location of pressure sensors in the BC for the long and short damper configurations. In all cases, the sensors are flush mounted with the inner BC face, facing directly into the film land or groove. Figure 17 shows a sketch of the top view of the pressure sensors radial location for both configurations [35].
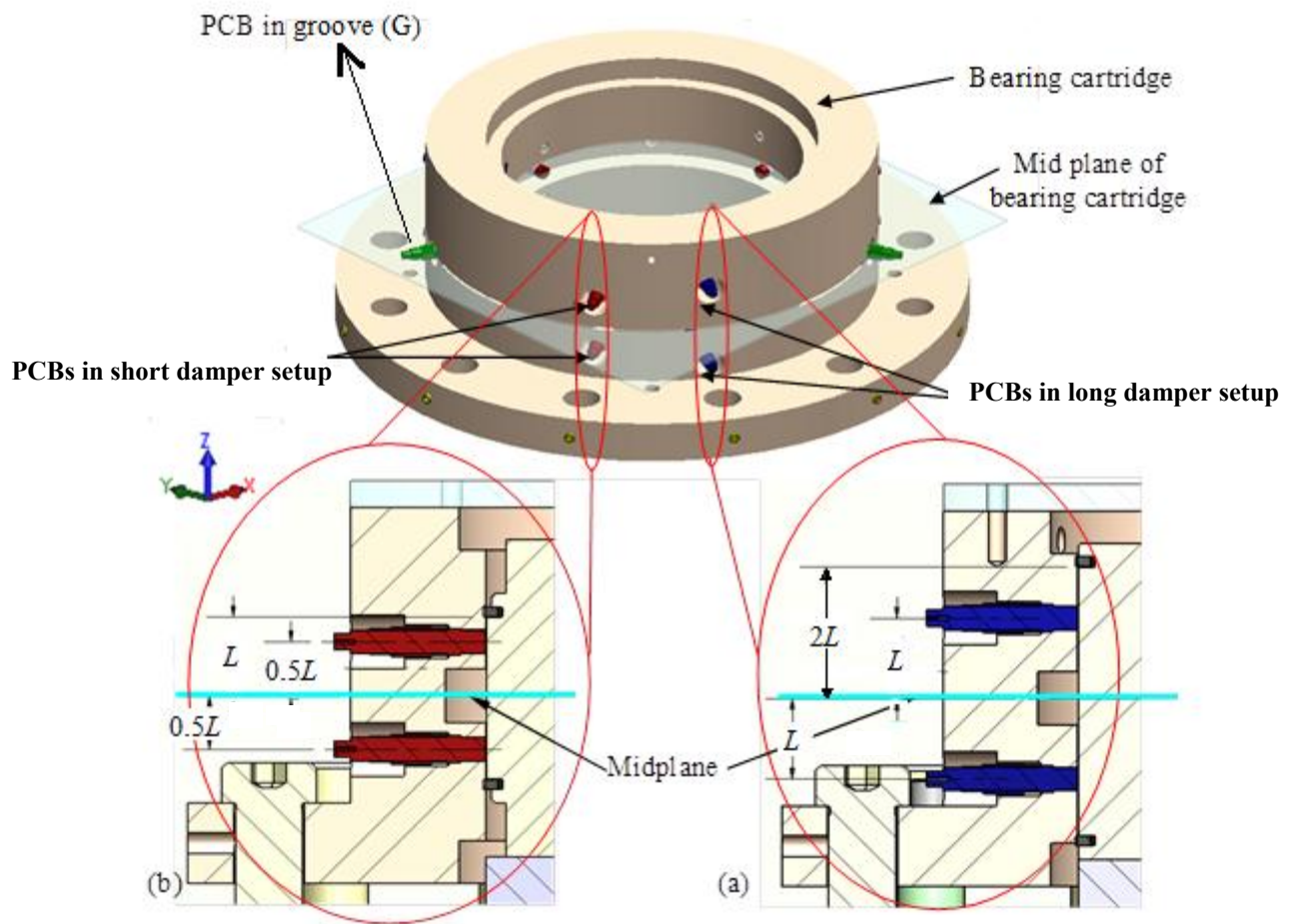
Figure 16. Disposition of pressure sensors in bearing cartridge. Cutaway views of bearing housing with pressure sensors placement for (a) long damper: land lengths 2*L*, and (b) short damper: land lengths *L* [35]
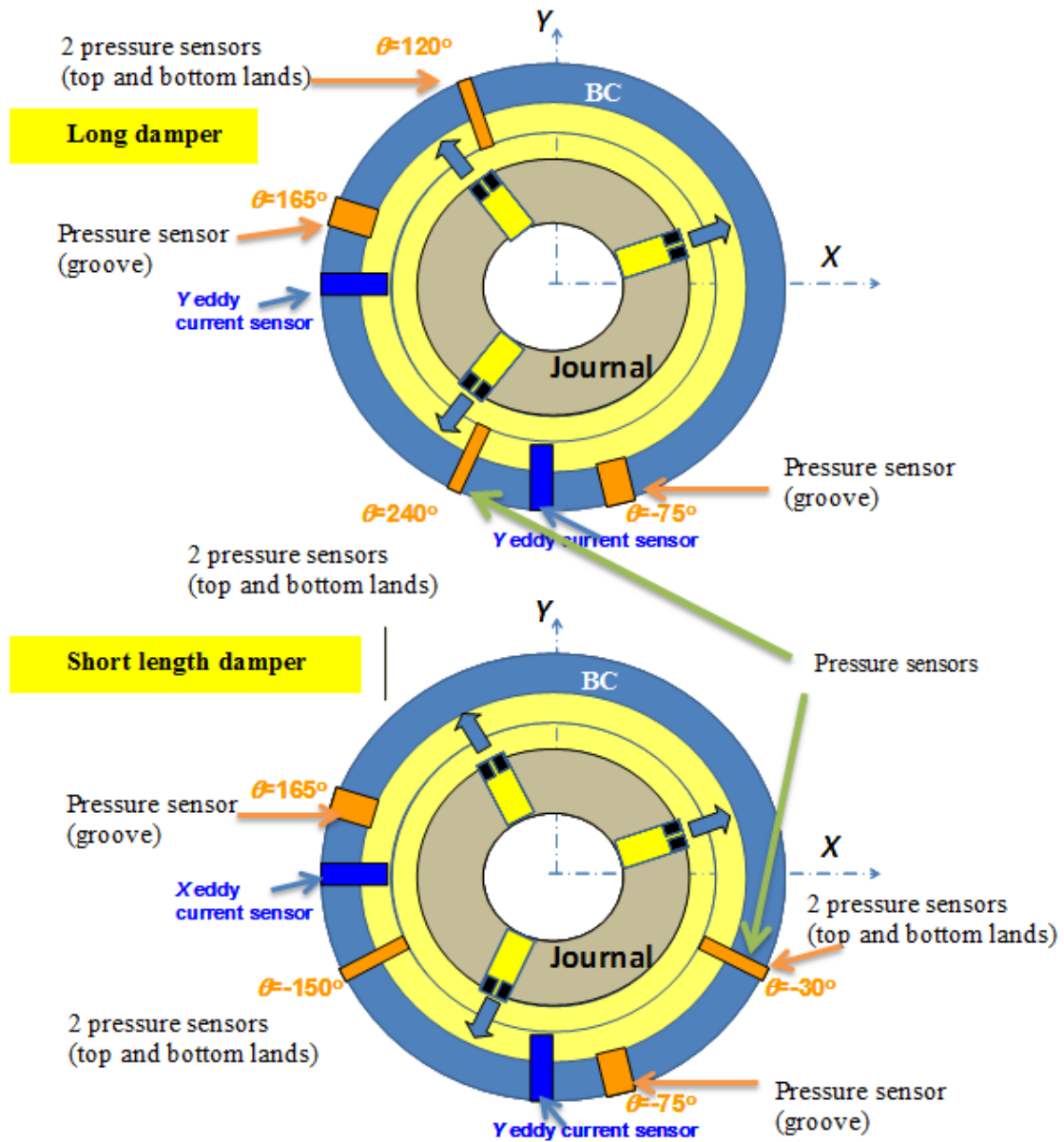
Figure 17. Circumferential location of dynamic pressure sensors in bearing cartridge for long and short length SFD configurations

Note that the DAQ board reads the sensor outputs, after the sensor signals are conditioned by the PCB [®] signal conditioners.

For the open ends long damper, the following figures show sample dynamic pressures recorded in the two film lands and groove while the BC describes circular centered orbits of amplitude $r \approx 0.1c_A$.

Figure 18 depicts pressures in the film lands for four periods of whirl motion and two excitation frequencies. Note that the period of whirl motion is $T_p = 2\pi/\omega$. The sensors are located in the top and bottom film land midplane at $\theta = 120^o$. Note that film pressures in the top and bottom film lands are nearly identical, hence showing both lands are of similar radial clearance and the BC is not tilted. At high excitation frequencies (250 Hz), high frequency spikes are observed in the pressure signal time traces, evidencing the occurrence of mild air ingestion, i.e., presence of ambient air in the lubricant.

Figure 19 shows dynamic pressures measured in the groove at $\theta = 165^o$ and $\theta = 285^o$ at two excitation frequencies. The groove pressures are as large as the film land pressures thus evidencing a significant influence of the groove on the forced response of the SFD. That is, the groove is not merely a source of lubricant that isolates the adjacent film lands, but contributes significantly to the SFD force performance [28].

Figure 20 show peak-peak pressures in the film lands and in the central groove versus whirl frequency. The magnitudes of dynamic film pressures linearly increase with whirl frequency, as expected. The groove pressures are of similar magnitudes to those in the film lands, as also observed in the time traces [35].
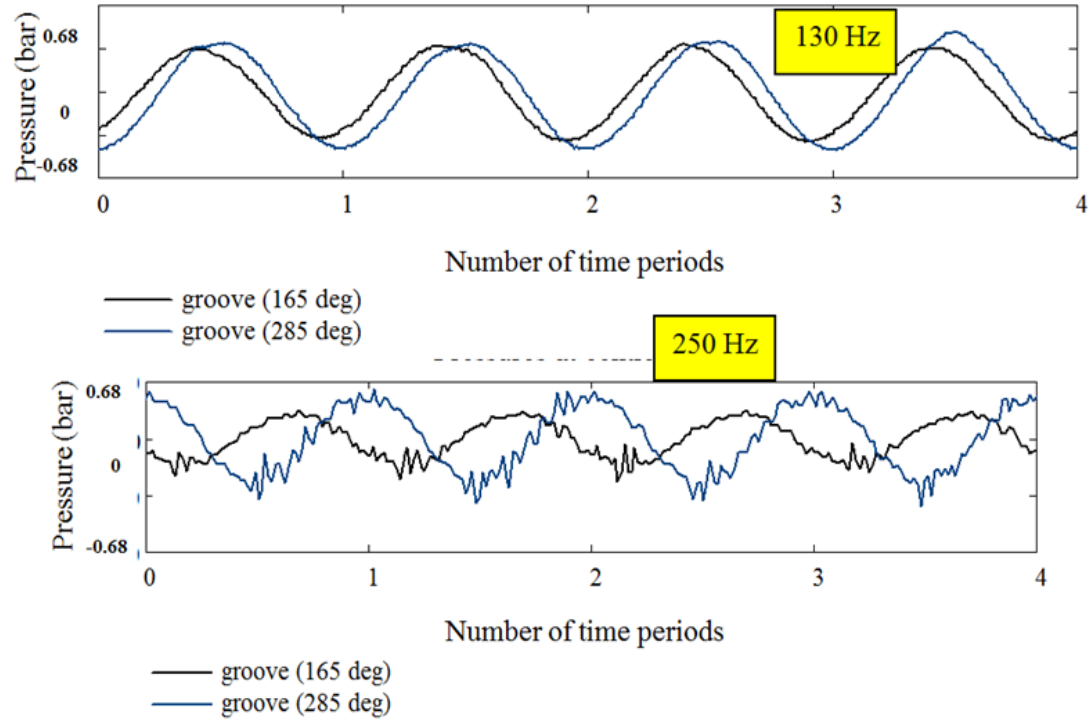
Figure 18. Long open ends SFD. Dynamic pressures in film lands at θ =120° (top and bottom film lands). Whirl frequency (a) 130 Hz (b) 250 Hz. Centered BC (e_s=0), circular orbit r= 0.1 c_A. Groove pressure P_G = 0.72 bar
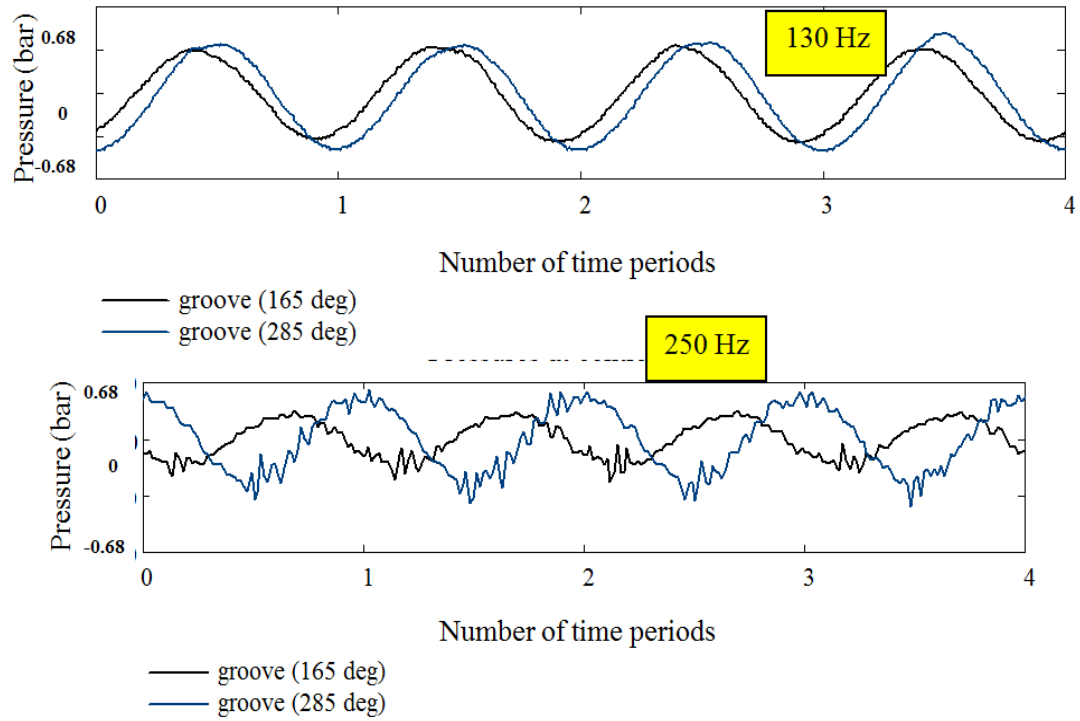
Figure 19. Long open ends SFD. Dynamic pressures in central groove at θ =165° and 285°. Frequency (a)130 Hz (b) 250 Hz. Centered Bearing e_s=0, circular orbit r=0.1 c_A. Groove pressure P_G = 0.72 bar
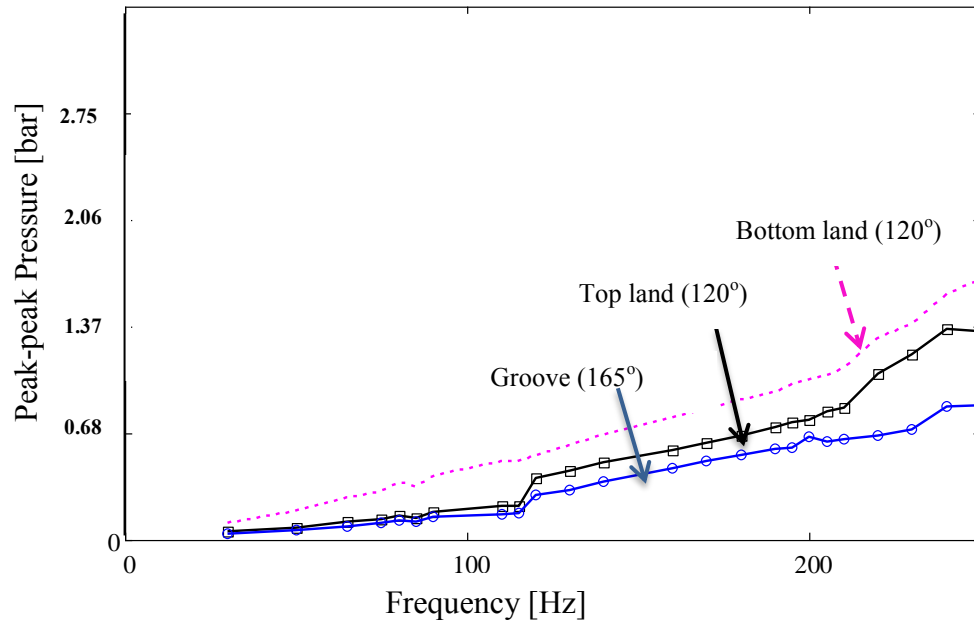
Figure 20. Long open ends SFD. Peak-peak pressures in film lands and in central groove versus whirl frequency. Centered Bearing e_s=0, circular orbit r=0.1c_A. Groove pressure P_G = 0.72 bar

CHAPTER IX

**IDENTIFICATION OF LUBRICATED SYSTEM AND SFD FORCE
COEFFICIENTS FOR THE LUBRICATED DAMPERS**

Figure 21 depicts a cross section of the damper and illustrates the path of lubricant flow through the test section. On identification of dry structure mechanical parameters, the test section is flooded with ISO VG 2 lubricant at room temperature (25°C). The lubricant enters the journal through a vertical feed pathway and exits into the central groove via three orifice restrictors, each of diameter 2.54 mm, and located 120° apart. The lubricant then flows through the top and bottom open ends SFD lands and exits to ambient. Table 6 lists the operating conditions for the long and short, open ends dampers.
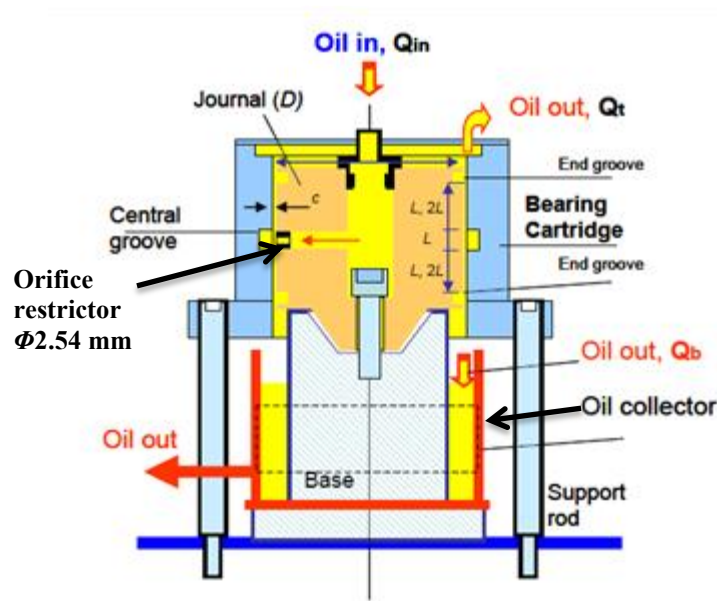
Figure 21. Cross section view of SFD test rig and lubricant flow path through damper film lands [31]

Table 6. Test parameters and operating conditions for measurements with open ends, long and short dampers

ISO VG 2 oil		
Viscosity at 23° C		0.00296 Pa·s
Density		784 kg/m^3
Vapor pressure		-1 bar
Diameter		D
Central groove Length		$L_G = L$
Groove depth		$d_G = \frac{3}{4} L$
	Short journal (B)	Long journal (A)
Land length	L	$2L$
Total length, L_T	$2L+L_G$	$4L+L_G$
Radial clearance, c	c_B	c_A
Static eccentricity, e_S	0-0.66 c_B	0- 0.36 c_A
Supply pressure, P_S	0.51 bar (gage)	0.72 bar (gage)
Groove static pressure, P_G	NA*	0.2 bar (gage)
Discharge pressure, P_A	0 bar (gage)	0 bar (gage)
Flow rate, Q_{in}	4.92 liters/min	4.92 liters/min

* Pressure sensor was not installed in the groove

The identification procedure for dry and lubricated system tests uses the recorded forces $F_{i,\ (i=X,Y)}$ and ensuing BC displacements $X_{i,\ (i=X,Y)}$ to render flexibility functions $G_{ij} = dX_i/dF_{j,\ (i,j=X,\ Y)}$. The flexibility functions of the lubricated system differ vastly from those of the dry system[6]. As an example, Figure 22 shows the flexibility functions G_{ij} vs. excitation frequency for the short length damper (land lengths L). The top graphs show flexibility functions for the dry system and the bottom figures those of the lubricated system. The continuous curves depict the model curve fits to the experimental flexibility functions. The vertical lines on the graphs depict the start (f_{start}) and end (f_{end}) frequencies of the IVF frequency identification range. Note the difference in scales for the top and bottom graphs. The figures make evident a very low damping ratio for the dry system ($\zeta_S < 0.05$) and a large damping ratio for the lubricated system ($\zeta \approx 0.3$). The damped natural frequency of the system drops when lubricated due to the squeeze film

---

[6] The flexibility functions for the lubricated short length damper include the BC mass, while those for the lubricated long damper exclude the BC mass

and more importantly, due to a large added mass arising from the lubricant in the film lands and groove. Note that the cross coupled flexibilities are a small fraction of the direct ones, i.e., $|G_{XY}|$, $|G_{YX}| << |G_{XX}|$; hence the squeeze film cross-coupled damping and cross-coupled inertia coefficients are negligible.
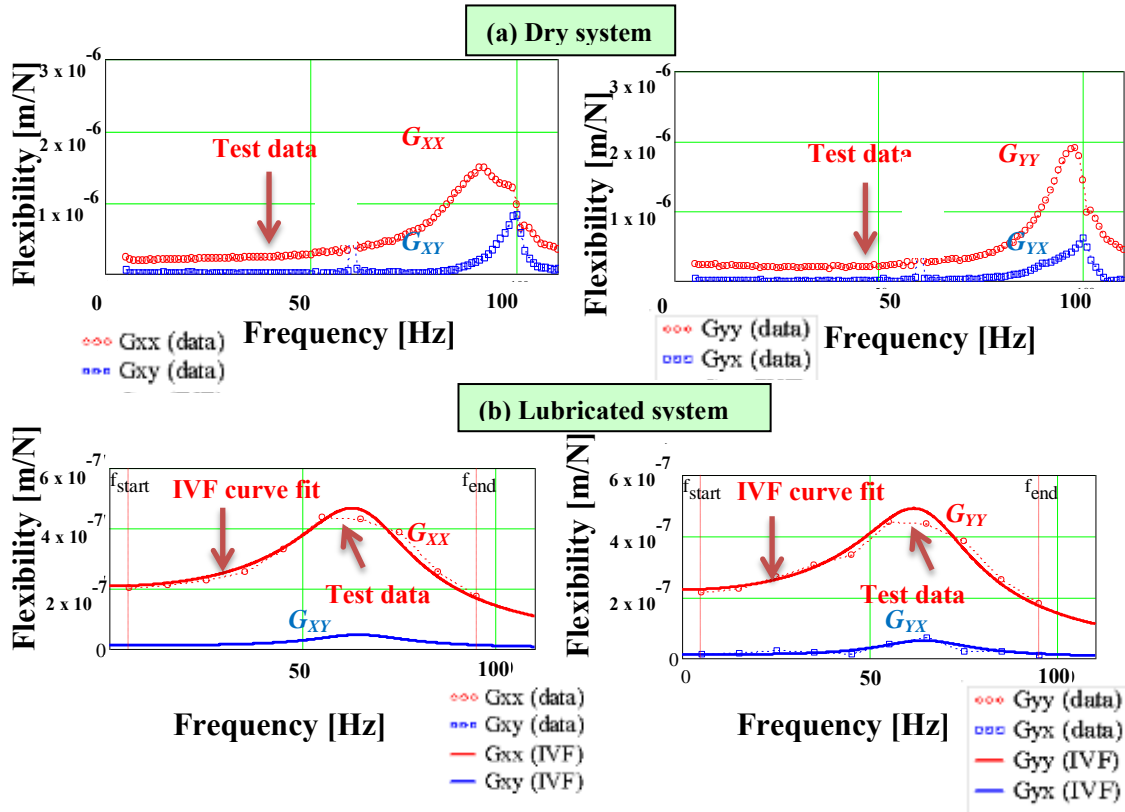
Figure 22. Short length open ends damper . Experimental and model curve fit flexibility functions G_{XX} and G_{XY} (left) G_{YY} and G_{YX} (right) for (a) dry system (b) lubricated system. Circular centered orbits of amplitude 0.09c_A. Note the difference in vertical scales

During the measurements on the lubricated system, the static loader pulls the BC to various off center positions. At each off-centered position, the orthogonally positioned shakers single frequency loads on the BC to produce either unidirectional, circular or elliptical orbits, as shown schematically in Figure 23. In the figure, e_S denotes the BC

static eccentricity, r the amplitude of a circular orbit, and ΔX and ΔY the amplitude of whirl for elliptical orbits.

(a) Unidirectional motion   (b) Circular orbit   (c) Elliptical orbit 2:1 amplitude ratio   (d) Elliptical orbit 5:1 amplitude ratio
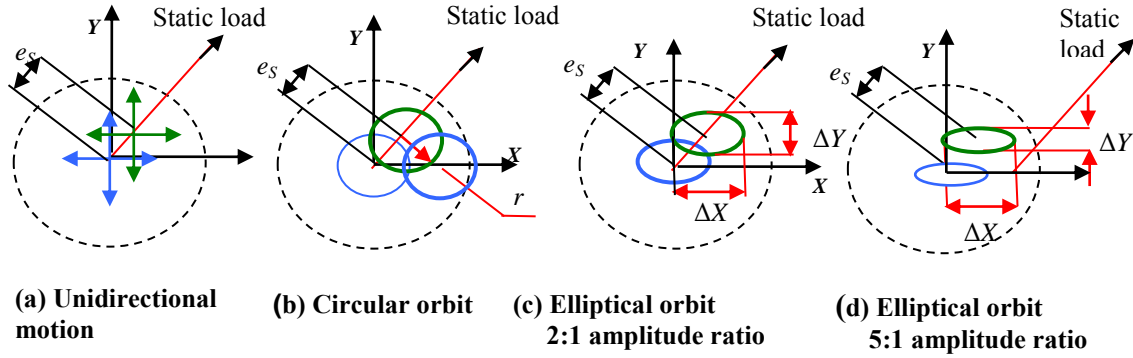
Figure 23. Schematic views of induced BC whirl motions, centered (blue) and off-centered (green). (a) Rectilinear displacements (b) circular orbits (c) Elliptic orbits, 2:1 amplitude ratio (d) elliptical orbits, 5:1 amplitude ratio. Dotted line represents clearance circle

IX.1 Force coefficients for the short length damper

Force coefficients for the short length damper are obtained from unidirectional and circular orbit tests over a frequency range 5- 95 Hz [9].

Figure 24 shows typical curve fit of real and imaginary parts of the impedance function $\mathbf{H} = \mathbf{G}^{-1}$. The real part of the impedance function is modeled as $\mathrm{Re}(H_{ij}) = K_{ij} - M_{ij}\omega^2$ and the imaginary part as $\mathrm{Im}(H_{ij}) = C_{ij}\omega$, where ω is operating frequency (rad/s). Note that the mass M includes the BC mass and SFD added mass. The high correlation factors ($r^2 > 0.95$) of the real and imaginary part curve fits with experimental data indicate the goodness of the chosen physical model. Note that the imaginary part of the impedance function $\mathrm{Im}(H_{ij}) = C_{ij}\omega$, is a line with a constant positive slope, evidencing that the damping coefficients are constant over the frequency range ,i.e., the damping is of viscous nature.
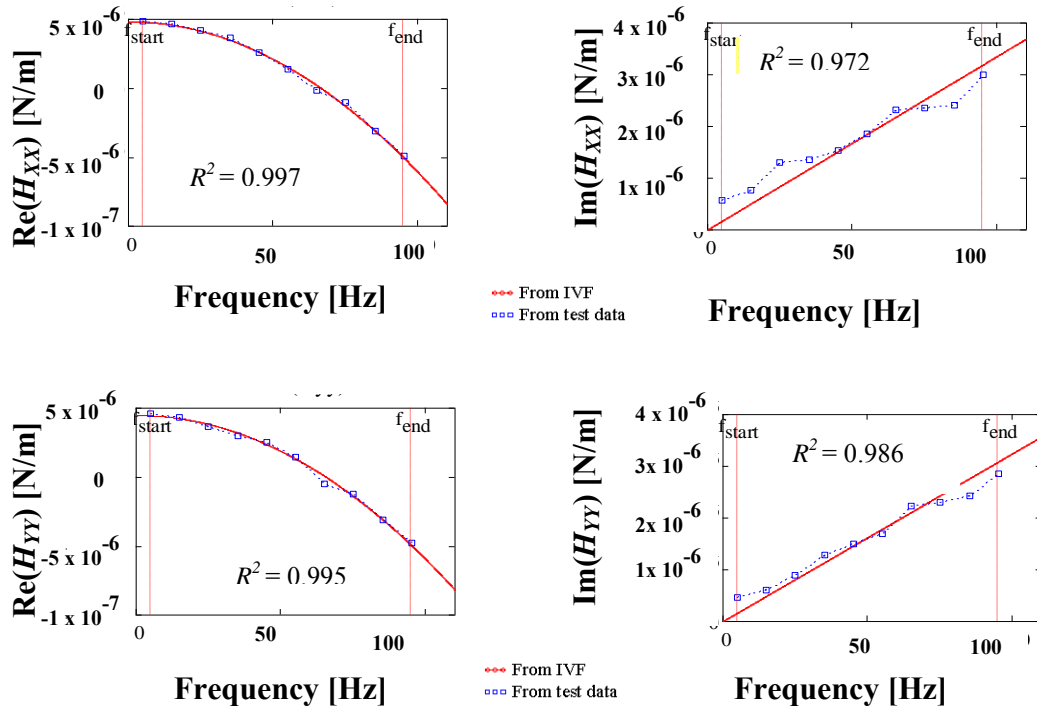
Figure 24. Short length open ends <u>lubricated</u> damper, circular orbits (r= 0.06 c_B). Real (left) and imaginary (right) parts of the experimental and IVFM impedances H_{ij}. Goodness of fit (R^2) shown. Identification range 5 – 95 Hz

Figure 25 depicts the squeeze film direct damping $(\overline{C}_{XX}, \overline{C}_{YY})_{SFD}$ and direct added mass $(\overline{M}_{XX}, \overline{M}_{YY})_{SFD}$ coefficients for the short length damper versus orbit amplitude (r), at centered ($e_S = 0$) and two static off-center positions ($e_S = 0.29c_B$ and $0.44c_B$). Recall that the SFD force coefficients are normalized respect to the values listed in Table 5. The cross-coupled coefficients are a minute fraction of the direct ones and hence not shown. The direct damping coefficients $(\overline{C}_{XX}, \overline{C}_{YY})_{SFD}$ first decrease and then increase with motion amplitude (maximum $0.66c_B$). The damping coefficients are nearly isotropic, i.e., $\overline{C}_{XX_{SFD}} \approx \overline{C}_{YY_{SFD}}$ for similar static eccentricities and amplitudes of motion. The direct

inertia coefficients $(\bar{M}_{XX}, \bar{M}_{YY})_{SFD}$ decrease with amplitude of motion, as theory also predicts [1].

SFD coefficients identified from circular and rectilinear (unidirectional) BC motions are nearly the same, denoting the damper insensitivity to the type of journal motion. Force coefficients from unidirectional motions are not shown for brevity.
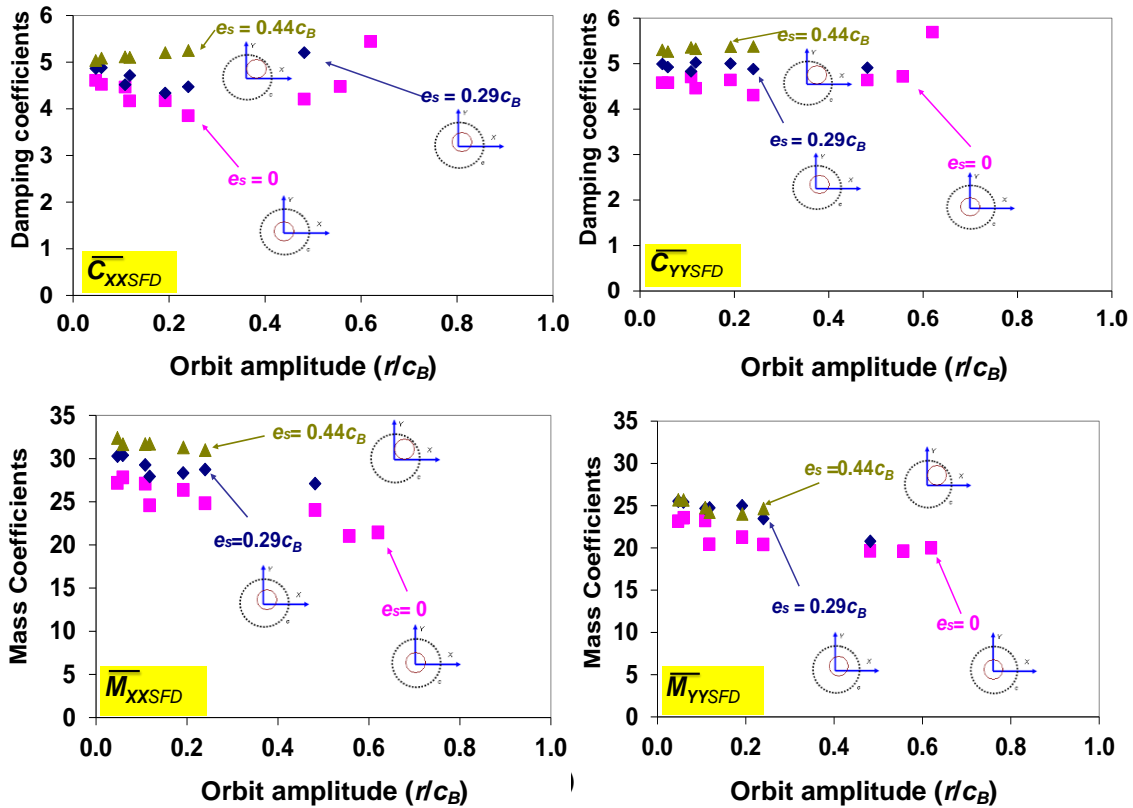
Figure 25. Short length open ends damper. Direct damping $(\bar{C}_{XX}, \bar{C}_{YY})_{SFD}$ **and added mass** $(\bar{M}_{XX}, \bar{M}_{YY})_{SFD}$ **coefficients versus amplitude (r) of circular orbit. Tests at centered condition (es=0) and two static eccentricities, es=0.29cB and 0.44cB**

Figure 26 and Figure 27 depict the SFD direct damping $(\bar{C}_{XX}, \bar{C}_{YY})_{SFD}$ and inertia $(\bar{M}_{XX}, \bar{M}_{YY})_{SFD}$ force coefficients versus static eccentricity (e_S). The experimental damping coefficients are isotropic, i.e., $\bar{C}_{XX_{SFD}} \approx \bar{C}_{YY_{SFD}}$ and increase moderately with static eccentricity. Note that the magnitudes of the test damping coefficients $(\bar{C}_{XX}, \bar{C}_{YY})_{SFD}$ fall in between 4 and 5, implying larger magnitudes than predictions derived from a classical lubrication analysis for the short length damper (see Table 5).

The added mass coefficients vary little with static eccentricity (e_S), see Figure 26. The added mass $\bar{M}_{YY_{SFD}}$ is consistently greater than $\bar{M}_{XX_{SFD}}$, by ~30%. For all the test data, the uncertainties in the identified coefficients are less than 5% and are too small to be depicted with uncertainty bars. See Appendix B for details on the uncertainty analysis.

Figure 26. Short length open ends damper. Direct damping $(\bar{C}_{XX}, \bar{C}_{YY})_{SFD}$ **coefficients versus static eccentricity ratio (e_s/c_B). Parameters identified from small amplitude ($r \approx 0.1c_B$) circular orbit tests, at a centered condition (e_s=0) and two static eccentricities, e_s=0.29c_B and 0.44c_B**
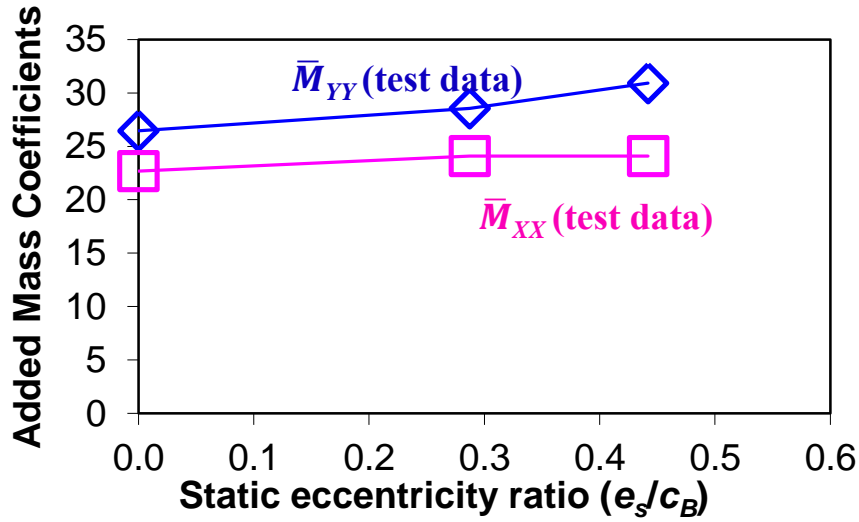
Figure 27. Short length open ends damper. Direct added mass $(\bar{M}_{XX}, \bar{M}_{YY})_{SFD}$ **coefficients versus static eccentricity ratio** (e_s/c_B)**. Parameters identified from small amplitude** $(r \approx 0.1c_B)$ **circular orbit tests, at a centered condition** $(e_s=0)$ **and two static eccentricities,** $e_s=0.29c_B$ **and** $0.44c_B$

The damping ratio (ζ) of the (lubricated) test system is the ratio of the identified damping coefficient (C) to the critical damping (C_C), i.e.,

$$\xi = C/C_c \tag{27}$$

Note that $C_c = 2M\omega_n$, where M is the identified lubricated system mass[7], and ω_n is the natural frequency of the test system.

The damping coefficient (C) and lubricated system mass (M) are a function of the amplitude of motion (r) and static eccentricity (e_S), as illustrated above; hence ζ varies with damper operating conditions. The range of ζ is 0.23 to 0.27, a significant increase over the dry structure damping ratio $(\zeta_S \approx 0.05$, see Table 3).

---

[7] Includes the BC effective mass (M_S) and added mass from the squeeze film (M_{SFD})

IX.2 Force coefficients for the long damper

Force coefficients for the long damper are obtained from circular and elliptic orbit tests over a frequency range spanning f_{start} =110 Hz and f_{end} = 210 Hz, using the IVFM. For circular motions, the whirl motion amplitudes are $\Delta X = \Delta Y$=0.045c_A and 0.09c_A. For elliptical orbits, the amplitude ratios are $\Delta X/\Delta Y$=2:1 with ΔX= 0.045c_A and 0.09c_A; and $\Delta X/\Delta Y$=5:1, with ΔX=0.045c_A and 0.09c_A. Note that the largest amplitude of motion is always along the X axis for elliptical orbits. Figure 23 depicts a schematic view of the induced circular and elliptical orbits.

Figure 28 shows the real and imaginary part curve fit of the impedance functions for the long damper. The real part is modeled as Re(H_{ij})= $K_{ij} - M_{ij}\omega^2$, where K_{ij} is the lubricated damper stiffness and M_{ij} includes both the residual mass $M_{rS_{ij}}$ and the SFD added mass $M_{SFD_{ij}}$. The imaginary part Im(H_{ij}) = $C_{ij}\omega$ has a constant slope, evidencing a uniform damping coefficient of viscous nature over the frequency range.

A close match between the experimental data points and the IVFM curve fit (R^2 >0.95) over a frequency range 110 – 210 Hz[8] evidences the goodness of the chosen physical model.

---

[8] The test data points in Figure 28 show a consistent trend over the range 110 – 210 Hz and deviate significantly beyond 210 Hz. Hence, the frequency range of identification is chosen as 110 – 210 Hz.
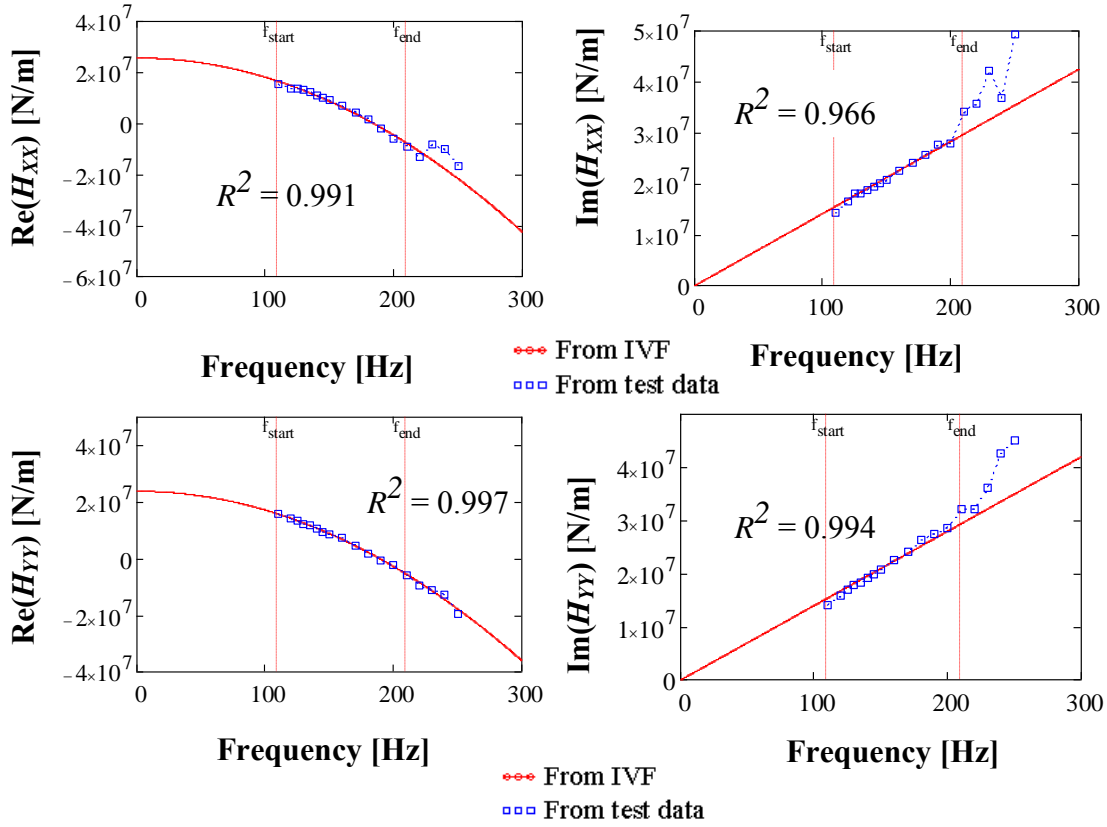
Figure 28. Long lubricated open ends damper. Circular orbits (r= 0.18 c_A). Real (left) and imaginary (right) parts of the experimental and IVFM impedances H_{ij}. Goodness of fit (R^2) shown. Identification range 110 – 210 Hz
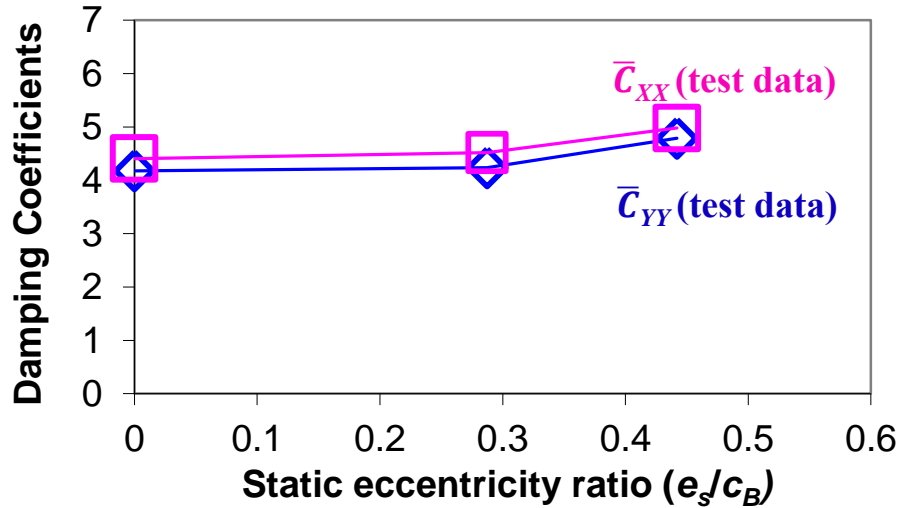
Figure 29 shows the direct damping $(\bar{C}_{XX}, \bar{C}_{YY})_{SFD}$ and added mass $(\bar{M}_{XX}, \bar{M}_{YY})_{SFD}$ coefficients for the long damper identified from circular orbit and elliptical orbit tests. The damping and added mass coefficients are identical for both amplitudes of motion as well as orbit shapes (circular, elliptical orbits with 2:1 and 5:1 amplitude ratios). Hence, the SFD forced response is independent of the BC kinematics.

The direct damping coefficients increase moderately with static eccentricity ($e_S = 0$, $0.23c_A$, $0.37c_A$) while the added mass coefficients are nearly constant with static eccentricity. The cross-coupled coefficients are a negligibly small fraction of the direct coefficients and hence not shown. Negligible cross-coupled damping coefficients

indicate that the damper operates without oil cavitation [1], as also confirmed by the film pressure measurements made in the film lands and groove. See section VII for film pressure measurements.
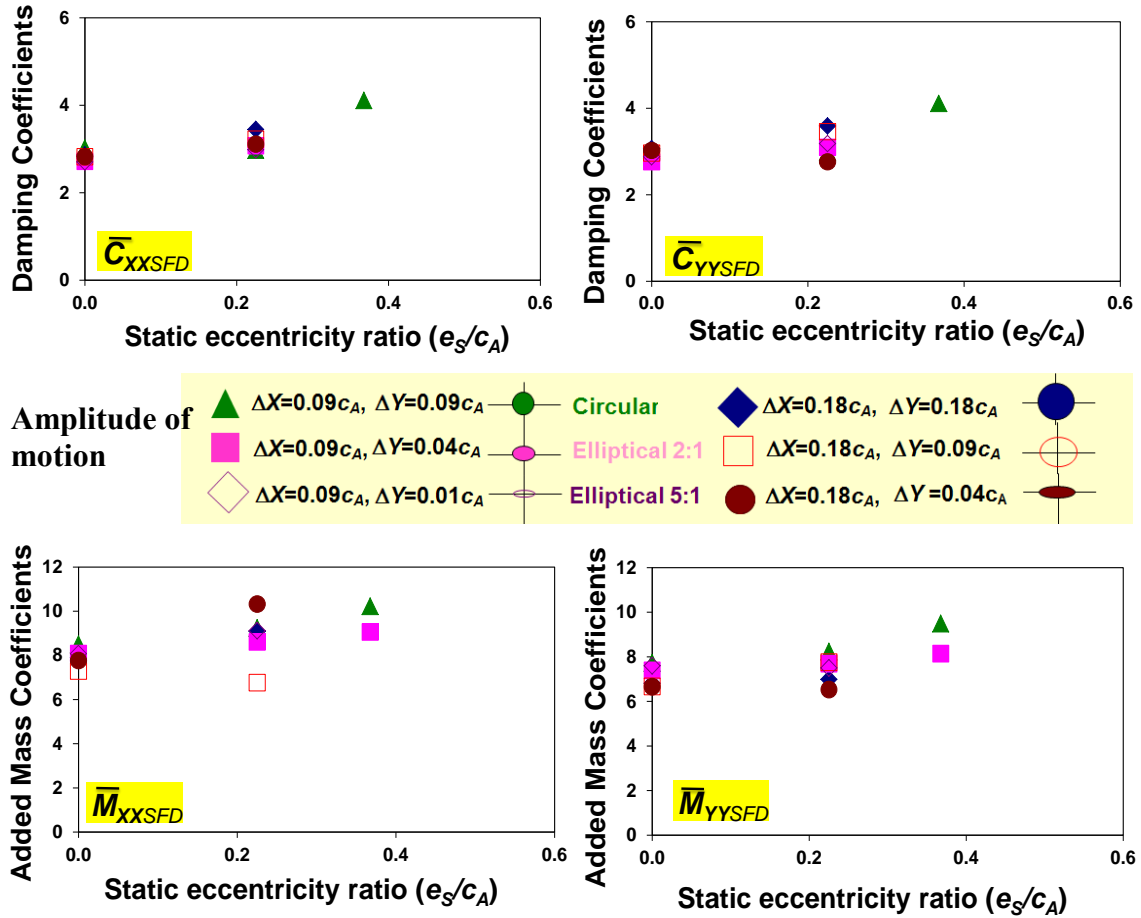
Figure 29. Long open ends damper. Top: Direct damping $(\bar{C}_{XX}, \bar{C}_{YY})_{SFD}$ and bottom: added mass $(\bar{M}_{XX}, \bar{M}_{YY})_{SFD}$ coefficients versus static eccentricity (e_S). Test data obtained for circular orbits: $\Delta X = \Delta Y = 0.045c_A$ and $0.09c_A$. For elliptical orbits: $\Delta X/\Delta Y = 2:1$ with $\Delta X = 0.045c_A$ and $0.09c_A$; and $\Delta X/\Delta Y = 5:1$, with $\Delta X = 0.045c_A$ and $0.09c_A$

Figure 30 and Figure 31 depict the SFD direct damping $(\bar{C}_{XX},\bar{C}_{YY})_{SFD}$ and inertia $(\bar{M}_{XX},\bar{M}_{YY})_{SFD}$ force coefficients versus the static eccentricity (e_S). The test force are derived for small amplitude circular motions $(r \approx 0.09 c_A)$ about a centered and two static off-centered positions $(e_S = 0.23 c_A, 0.37\ c_A)$.

The experimental damping coefficients are isotropic, ie., $\bar{C}_{XX_{SFD}} \approx \bar{C}_{YY_{SFD}}$ and increase moderately with static eccentricity. The added mass coefficients are nearly constant with static eccentricity (e_S). The large magnitudes of test added mass coefficients, i.e., $(\bar{M}_{XX},\bar{M}_{YY})_{SFD} \approx 8$ evidence that the central groove, disregarded in a conventional analysis, plays an important role in enhancing the fluid inertia effect of the whole SFD.
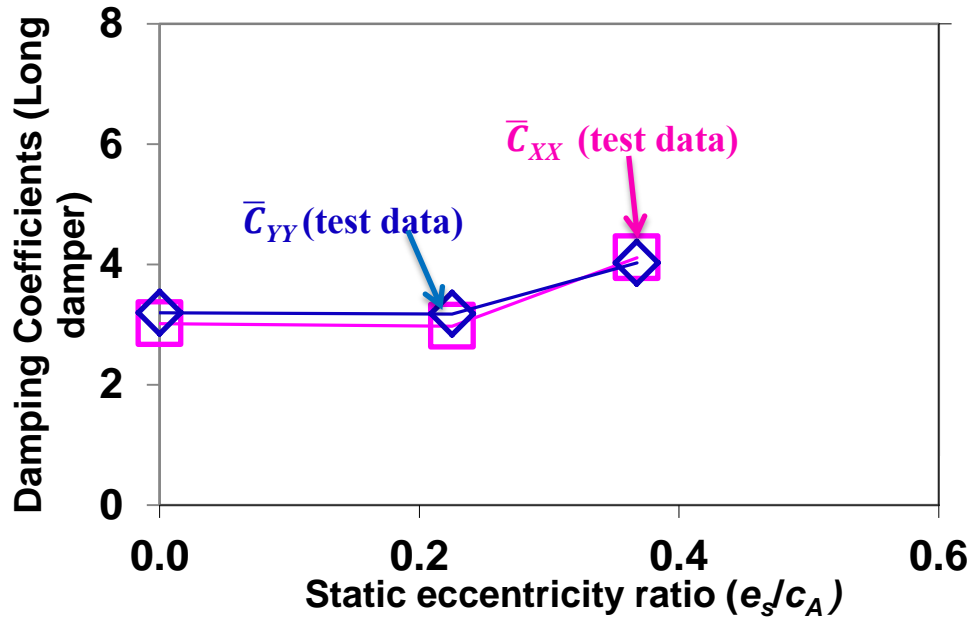
Figure 30. Long open ends damper. Direct damping $(\bar{C}_{XX},\bar{C}_{YY})_{SFD}$ coefficients versus static eccentricity ratio (e_s/c_A). Parameters identified from small amplitude ($r \approx 0.1c_A$) circular orbit tests, at a centered condition (e_s=0) and two static eccentricities, e_s=0.18c_A and 0.36c_A
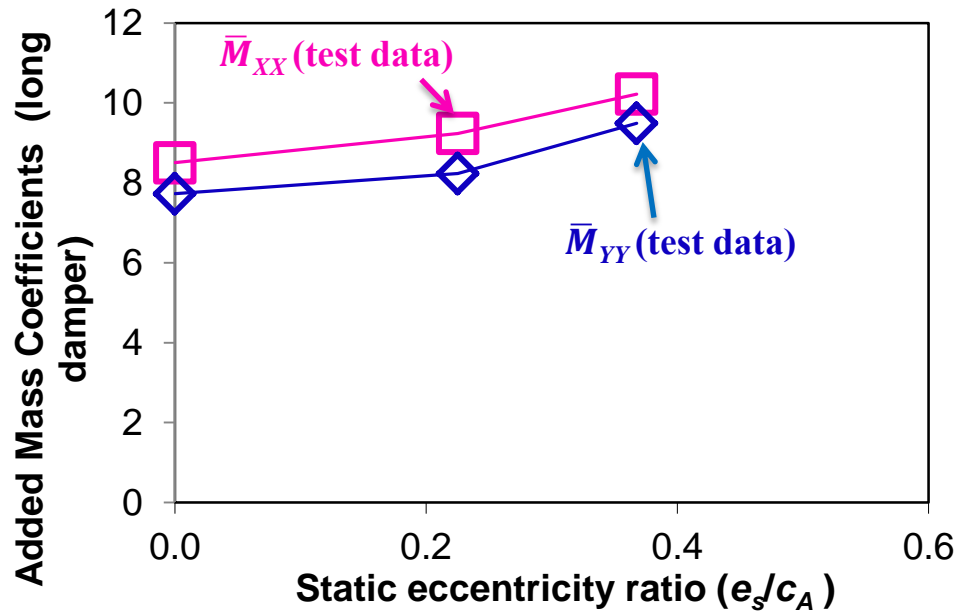
Figure 31. Long open ends damper. Direct added mass $(\bar{M}_{XX}, \bar{M}_{YY})_{SFD}$ **coefficients versus static eccentricity ratio (e_s/c_A). Parameters identified from small amplitude ($r \approx 0.1c_A$) circular orbit tests, at a centered condition ($e_s=0$) and two static eccentricities, $e_s=0.18c_A$ and $0.36c_A$**

The lubricated system damping ratio (ζ) lies between 0.4 and 0.55 for the long damper, a significant increase over the damping ratio of the corresponding dry structure ($\zeta_S \approx 0.03$, see Table 4).

CHAPTER X

COMPARISON OF TEST COEFFICIENTS WITH PREDICTIONS
OBTAINED FROM A COMPUTATIONAL ANALYSIS

The test force coefficients obtained from the short and long open ends dampers are compared with predictions obtained from a novel computational model developed by San Andrés [27] .

A Microsoft® Excel® user interface accepts user inputs and displays results generated by a FORTRAN® code implementing a finite element solution to the Reynolds equation. The code can model a multitude of SFD geometries and lubricant feed systems. Figure 32 depicts the current test SFD configuration that the code models. The figure also depicts the coordinate system [33].
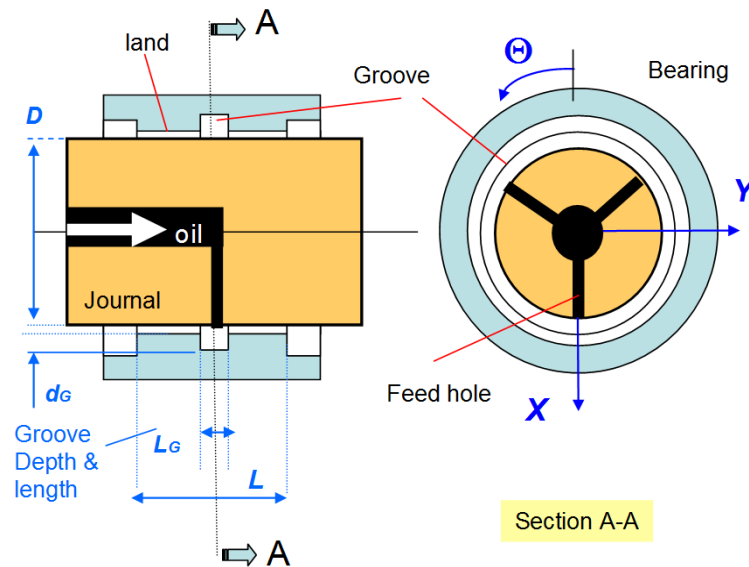
Figure 32. Current SFD geometry modeled in computational program PW_SFD_2010 [33]

The computational analysis solves the modified Reynolds equation [27]

$$\frac{\partial}{\partial x}\left(h^3 \frac{\partial P}{\partial x}\right)+\frac{\partial}{\partial z}\left(h^3 \frac{\partial P}{\partial z}\right)=12\,\mu\frac{\partial h}{\partial t}+6\mu R\Omega\frac{\partial h}{\partial x}+\rho h^2\,\frac{\partial^2 h}{\partial t^2} \tag{28}$$

where h and P are the film thickness and film pressure within the damper circumference and axial length, and (ρ,μ) are the lubricant viscosity and density, respectively. The modified Reynolds equation above accounts for temporal fluid inertia effects, applicable to small amplitude motions about a centered or eccentric static journal positions. The film thickness is

$$h_{(\Theta,z,t)}=c_{(z)}+e_{X_{(t)}}\cos(\Theta)+e_{Y_{(t)}}\sin(\Theta) \tag{29}$$

where $c_{(z)}$ is a step-wise clearance distribution along the axial direction and (e_X, e_Y) are the components of the journal center eccentricity.

The finite element method solves Eq. (28) and its first-order perturbations to give the force coefficients, see Ref. [36].

Figures 33 and 34 show predicted SFD direct damping $(C_{XX}=C_{YY})_{SFD}$ and inertia $(M_{XX}=M_{YY})_{SFD}$ force coefficients versus central groove depth (d_η) for the short length and long damper configurations, respectively. The predictions refer to a centered journal position $(e_s=0)$ for an SFD with three feed holes.

The predicted damping coefficients decrease monotonically as the groove depth increases, whereas the inertia force coefficients first increase for shallow groove depths, and later decrease for very deep groove depths. Note that the (normalized) damping and added mass predictions attain a value of 1 for large groove depths, hence approaching the predictions delivered by the formulas in Eq.(25). The figures also mark the experimental damping and inertia force coefficients. Note that the test data matches the predictions only at a particular groove depth.

Following Ref. [4], effective groove depths, much lesser than the physical groove depths, are selected for predictions of the force coefficients. The actual physical depth plays no role in the estimation for force coefficients. Test data and analysis, see Refs.[19], [37],[4], have shown consistently the force coefficients, in particular added masses, are strongly affected by the presence of central grooves. Shallow effective groove depths demonstrate that the grooves do not isolate the film lands.

The central groove does not merely act as a source or sink of fluid flow, and impervious to the generation of dynamic pressures. On the contrary, measurements of dynamic pressures in the groove show large magnitudes, as large as in the film lands [33]. See section VIII for a discussion of measured pressures.
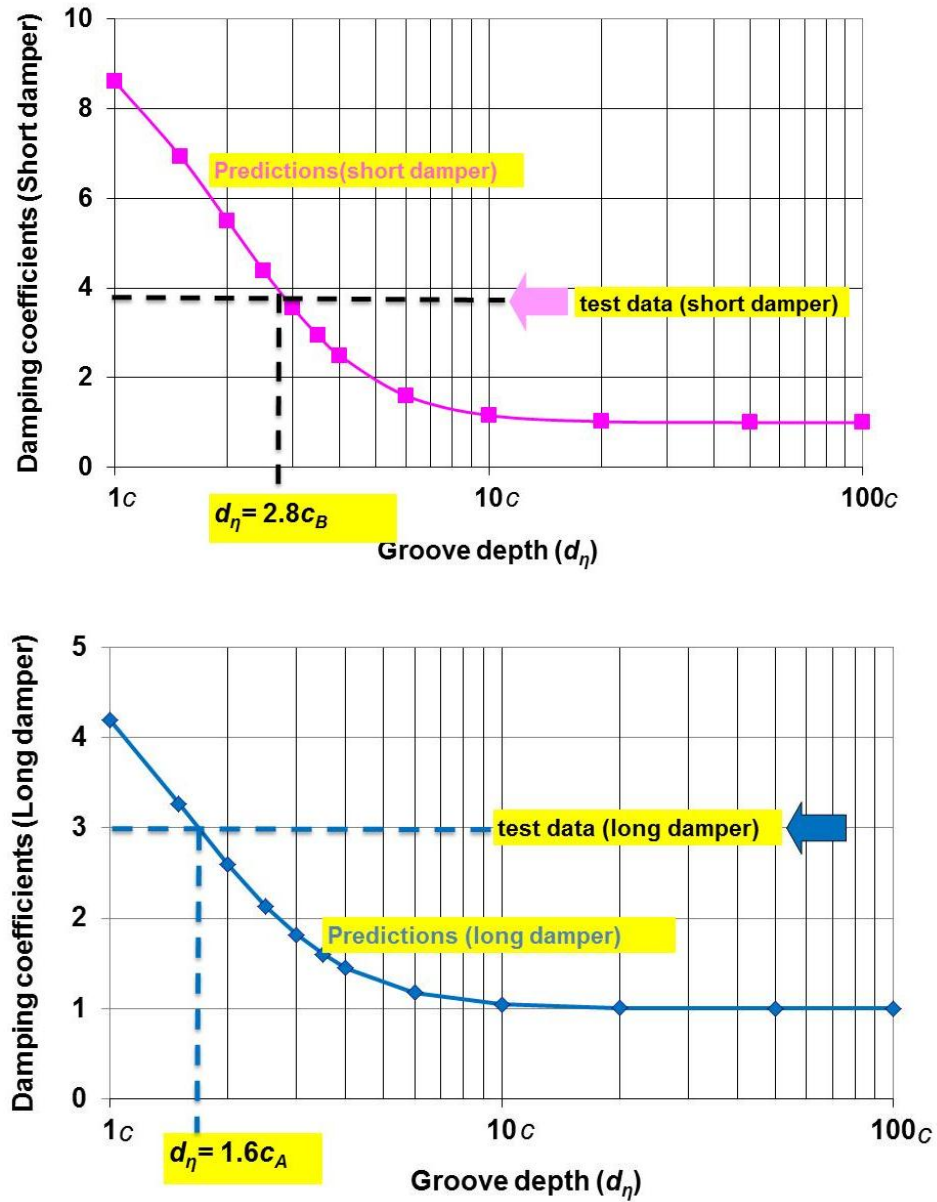
Figure 33. Predicted SFD damping coefficients $(\bar{C}_{XX}, \bar{C}_{YY})_{SFD}$ **versus groove depth for a centered damper (e_S=0). Short length damper (top) and long damper (bottom). Test data overlaid with predictions to estimate effective groove depth (d_η)**
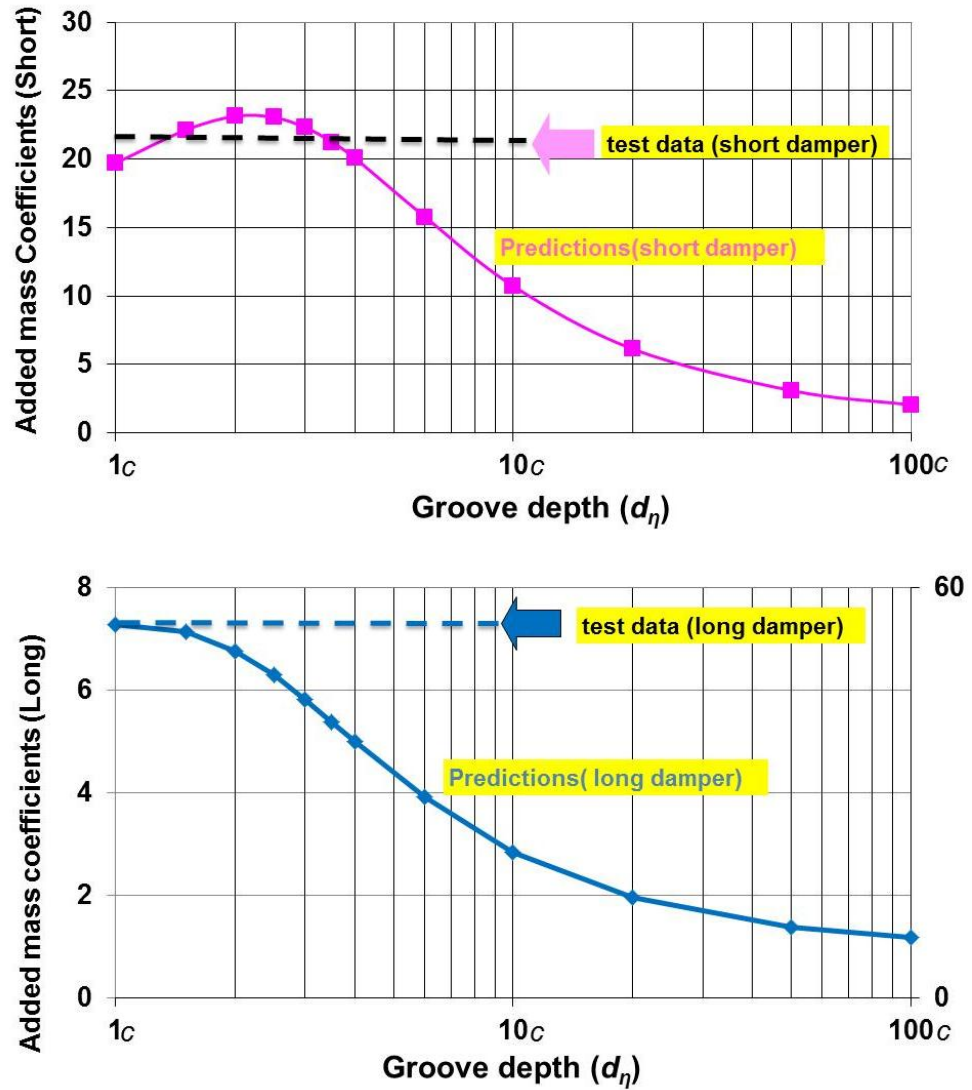
Figure 34. Predicted SFD added mass coefficients $(\bar{M}_{XX}, \bar{M}_{YY})_{SFD}$ **versus groove depth. Centered damper (e$_S$=0). Short length damper (top) and long damper (bottom). Test data overlaid with predictions**

Figures 35 and 36 show a comparison of the experimental and predicted damping and inertia force coefficients versus static eccentricity (e_s) for the short length and long dampers, respectively. Table 7 lists the inputs to the computer code to obtain predictions of force coefficients.

The test data is obtained from circular orbit tests of amplitude $r = 0.1c$ for both dampers. The predictions are obtained for effective groove depths $d_\eta = 2.8c_B$ and $1.6c_A$ for the short length and long damper configurations, respectively. Note that the actual physical groove depth is $\sim 75c$, while the effective depths are just a few times the film clearance, showing the central groove contributes significantly to the generation of force coefficients.

Table 7. Geometry, oil properties and operating conditions for prediction of SFD force coefficients

Parameter	Open ends short damper	Open ends long damper
Geometry - three feed holes 120° apart		
Journal Diameter	D	
Land Length	L	$2L$
Radial Land Clearance	c_B	c_A
Damper Axial Length (two lands plus groove, L_T)	$3L$	$5L$
Central Groove		
Effective depth, d_η	$2.8c_B$	$1.6c_A$
Axial length, L_G	L	L
Boundary conditions and fluid properties		
Groove pressure, P_G	0.52 bar	0.72 bar
Ambient pressure, P_a (gauge values)	0 bar	
Oil Cavitation pressure, P_{cav}	-1.01 bar	
Oil ISO VG2 supply temperature, T_{supply}	25 °C	
Dynamic Viscosity at T_{supply}, μ	0.00296 Pa·s	
Density, ρ	785 kg/m³	

The predicted direct damping coefficients agree very well with the test damping coefficients. Both increase moderately with static eccentricity for the short damper, and more rapidly for the long damper. The test coefficients are nearly isotropic, but the predicted coefficients are unequal (i.e., $\overline{C}_{YY} > \overline{C}_{XX}$).

The predicted added mass coefficients match well with the test derived coefficients for the short damper, and are underpredicted for the long damper. Both test and predicted coefficients remain unaffected by static eccentricity (e_S). Note that predicted $\overline{M}_{YY} > \overline{M}_{XX}$, for both dampers.

Neither the test results nor predictions show the presence of squeeze film cross-coupled damping coefficients, evidencing the complete absence of lubricant cavitation.

The goodness of correlation between experimental results and predictions is due to the novel computational SFD model that takes into account the flow interactions between the groove, lands and feed holes. As stated earlier, classical SFD lubrication analyses, disregarding the dominant effect of a feed groove, predict much lower damping and inertia force coefficients and match predictions from the current computational analysis for very large groove depths ($d_\eta \gg c$).
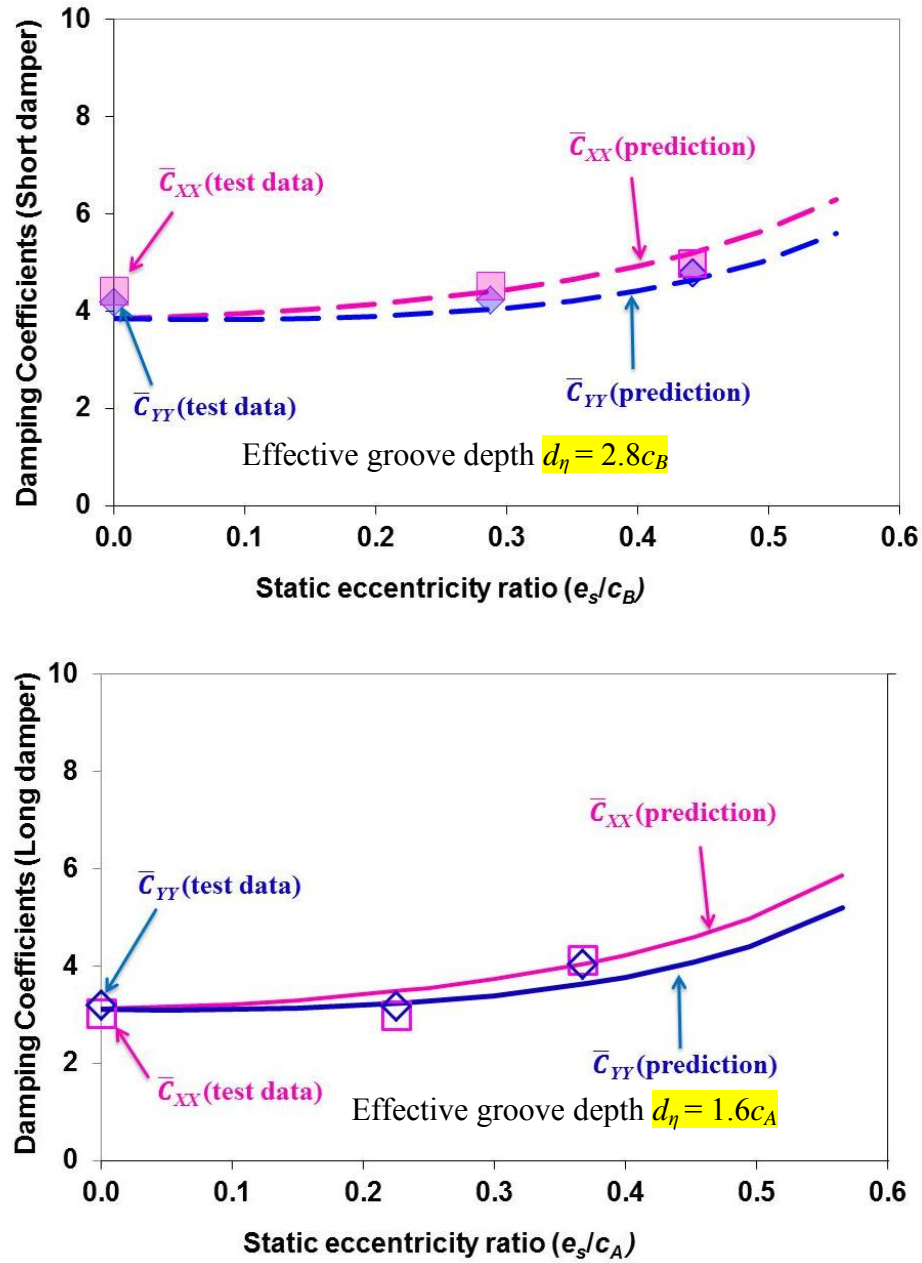
Figure 35. Short length and long open ends SFD: Test and predicted damping coefficients $(\bar{C}_{XX}, \bar{C}_{YY})_{SFD}$ versus static eccentricity (e_S/c). Effective groove depths: Short damper (top) $d_\eta = 2.8c_B$, long damper (bottom) $d_\eta = 1.6c_A$
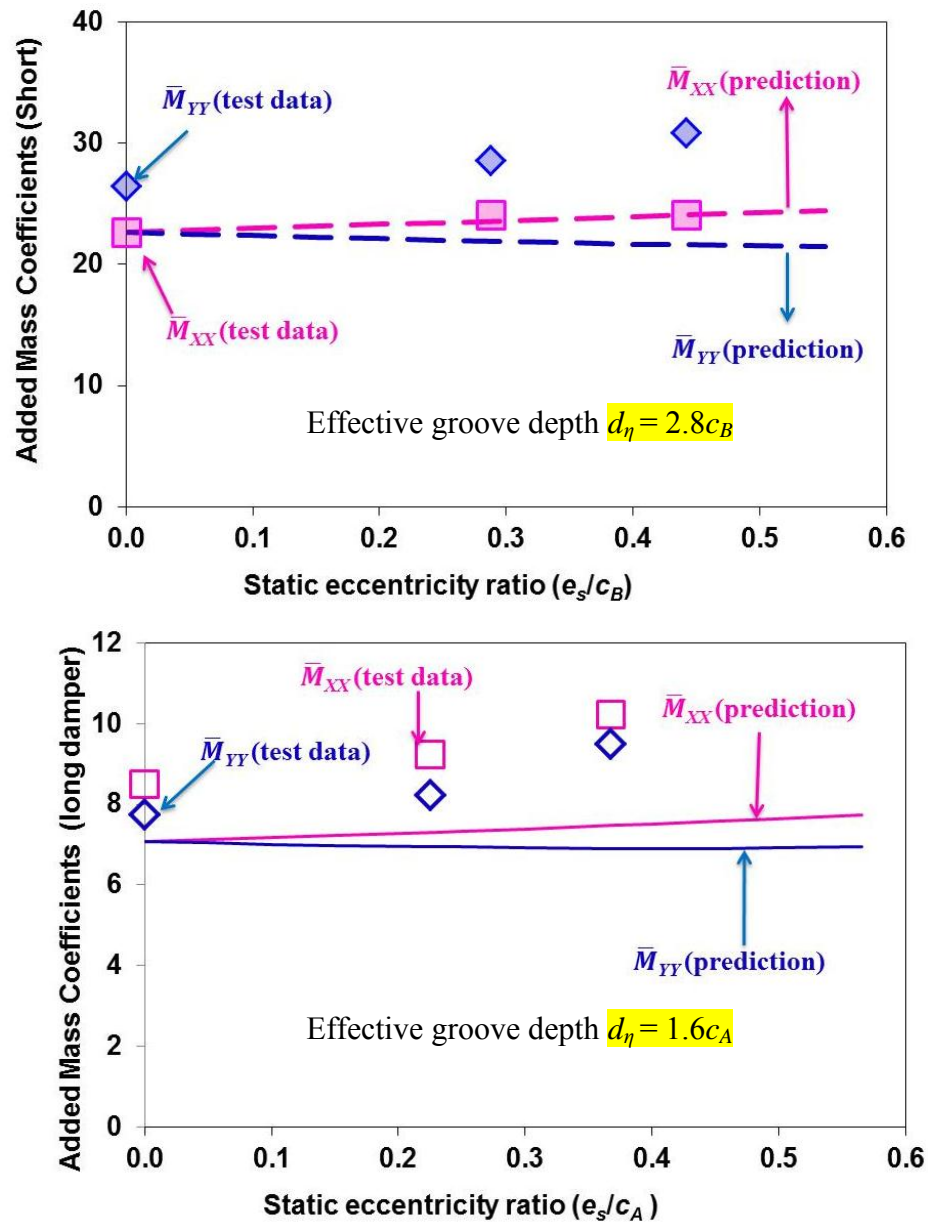
Figure 36. Short and long open ends SFD: test and predicted added mass coefficients $(\bar{M}_{XX}, \bar{M}_{YY})_{SFD}$ **versus static eccentricity. Effective groove depths: Short damper (top)** $d_\eta = 2.8c_B$**, long damper (bottom)** $d_\eta = 1.6c_A$

CHAPTER XI

OBSERVATIONS AND CONCLUSIONS

Dynamic load measurements were conducted on two open ends dampers, long and short. The short length damper has a soft support structure, and the long damper has a much stiffer support structure. A frequency domain parameter identification procedure identifies the test system and SFD force coefficients. The major observations derived from the measurements are [28, 35]

For the short length open ends SFD,
(two parallel dampers of land length L each, radial clearance c_B, support structure stiffness 6.13 MN/m, excitation frequency range 5 – 95 Hz)

(a) Direct damping coefficients are sensitive to the amplitude of circular motion (max $0.62c_B$) and increase mildly with the static eccentricity (e_s), max $0.44c_B$. Direct inertia coefficients decrease with the amplitude of whirl orbit (r) and increase mildly with the static eccentricity (e_s).

(b) The identified force coefficients remain unaffected by type of journal motion, rectilinear (unidirectional) or circular.

(c) The cross-coupled damping and inertia coefficients are a small fraction of the direct ones. Absence of cross-coupled damping coefficients indicates the absence of lubricant cavitation.

For the long open ends SFD,
(two parallel dampers of land length $2L$ each, radial clearance c_A, support structure stiffness 26.27 MN/m, excitation frequency range 110 –210 Hz)

(d) Direct damping coefficients increase moderately with the static eccentricity, max. $0.37c_A$, and are insensitive to the amplitude and type of journal motion, circular or highly elliptical, max. $0.18c_A$.

(e) Direct inertia coefficients decrease as the amplitude of whirl orbit increases. The inertia coefficients remain nearly invariant with static eccentricity (e_S).

(f) Due to a loose test rig installation, the journal also moves when the BC is excited by the shakers. A modified parameter identification procedure that uses measured BC accelerations delivers the force coefficients for the long damper

(g) The cross-coupled damping and inertia coefficients are a small fraction of the direct coefficients, and denote SFD operation without lubricant cavitation.

For both dampers,

(h) The measured pressures in the groove are as large in magnitude as those in the film lands, showing that the groove does not isolate the film lands but actually generates large damping and inertia reaction forces that contribute significantly to the forced performance of the test SFDs.

(i) Predictions from a SFD predictive tool [27] agree well with the test inertia and damping coefficients for both dampers when using shallow effective groove depths. The predictive tool incorporates a physical model that accounts for the flow interactions in the groove and film lands.

REFERENCES

[1]   San Andrés, L., 2010, "Squeeze Film Dampers: Operation, Models and Technical Issues," Modern Lubrication Theory, Notes 13, Texas A&M University Digital Libraries, https://repository.tamu.edu/handle/1969.1/93197. Accessed 02/05/2011.

[2]   San Andrés, L., 1992, "Analysis of Short Squeeze Film Dampers With a Central Groove," J.Tribol., **114**(4), pp. 659-664.

[3]   Arauz, G. L., and San Andrés, L., 1997, "Experimental Force Response of a Grooved Squeeze Film Damper," Tribol. Int., **31**(5), pp. 265-270.

[4]   Delgado, A., 2008, "A Linear Fluid Inertia Model For Improved Prediction Of Force Coefficients In Grooved Squeeze Film Dampers And Grooved Oil Seal Rings," PhD Dissertation, Texas A&M University, College Station, TX, December 2008.

[5]   San Andrés, L., 2008, "P&W SFD Test Rig: Design and Statement of Work for 2009- 2010," Design Report to Pratt & Whitney (United Technologies Corporation), December.

[6]   Della Pietra, L., and Adiletta, G., 2002, "The Squeeze Film Damper over Four Decades of Investigations. Part I: Characteristics and Operating Features," Shock Vib. Dig, **34**(1), pp. 3-26.

[7]   Tiwari, R., Lees, A.W., and Friswell, M.I., 2004, "Identification of Dynamic Bearing Parameters: A Review," Shock Vib. Dig, **36**(2), pp. 99-124.

[8]   Fritzen, C.-P., 1986, "Identification of Mass, Damping and Stiffness Matrices of Mechanical Systems," Journal of Vibration, Acoustics, Stress, and Reliability in Design. , **108**, pp. 9-16.

[9]   San Andrés, L., 2010, "Experimental Identification of Bearing Force Coefficients," Modern Lubrication Theory, Notes 14, Texas A&M University Digital Libraries, https://repository.tamu.edu/handle/1969.1/93197. Accessed 02/05/2011.

[10] Tichy, J. A., 1987, "A Study of the Effect of Fluid Inertia and End Leakage in the Finite Squeeze Film Damper," J.Tribol., **109**(1), pp. 54-60.

[11] Ramli, M. D., Roberts,J.B., and Ellis,J., 1987, "The Determination of Squeeze Film Dynamic Coefficients from Experimental Transient Data," J. Tribol., **109**(1), pp. 155-163.

[12] Ramli, M. D., Roberts,J.B., and Ellis,J., 1996, "Force Coefficients for a Centrally Grooved Short Squeeze Film Damper," J. Tribol., **118**(3), pp. 608-616.

[13] Ellis, J., Roberts, J. B., and Hosseini, S. A., 1990, "The Complete Determination of Squeeze-Film Linear Dynamic Coefficients from Experimental Data," J.Tribol., **116**(3), pp. 528-534.

[14] Zhang, J. X., Roberts, J. B., and Ellis, J., 1994, "Experimental Behavior of a Short Cylindrical Squeeze Film Damper Executing Circular Centered Orbits," J.Tribol., **116**(3), pp. 528-534.

[15] Arauz, G. L., and San Andrés L., 1996, "Experimental Study on the Effect of a Circumferential Feeding Groove on the Dynamic Force Response of a Sealed Squeeze Film Damper," J.Tribol., **118**(4), pp. 900-905.

[16] Qingchang, T., Xaohua, L., and Dawei, Z., 1998, "Analytical Study of the Effect of a Circumferential Feeding Groove on the Unbalance Response of a Rigid Rotor in a Squeeze Film Damper," Tribol. Int., **31**(5), pp. 265-270

[17] Qingchang, T., Ying, C., and Lyjiang, W., 1997, "Effect of a Circumferential Feeding Groove on Fluid Force in Short Squeeze Film Dampers," Tribol. Int., **30**(6), pp. 409-416.

[18] Lund, J. W., Myllerup, C. M., and Hartmann, H., 2003, "Inertia Effects in Squeeze-Film Damper Bearings Generated by Circumferential Oil Supply Groove," J. Vib. Acoust., **125**(4), pp. 495-499.

[19] Kim, K.-J., and Lee, C.-W., 2005, "Dynamic Characteristics of Sealed Squeeze Film Damper With a Central Feeding Groove," J. Tribol., **127**(1), pp. 103-111.

[20] Defaye, C., Arghir, M., Bonneau, O., Carpentier, P., Debailleux, C., and Imbourg, F., 2006, "Experimental Study of the Radial and Tangential Forces in a Whirling Squeeze Film Damper," Tribol. Trans., **49**(2), pp. 271 - 278.

[21] Gehannin, J., Arghir,M., and Bonneau,M., 2010, "Complete Squeeze-Film Damper Analysis Based on the "Bulk Flow" Equations," Tribol. Trans., **53**(1), p. 84.

[22] San Andrés, L., and De Santiago, O., 2004, "Forced Response of a Squeeze Film Damper and Identification of Force Coefficients From Large Orbital Motions," J. Tribol., **126**(2), pp. 292-300.

[23] San Andrés, L., and Delgado, A., 2007, "Identification of Force Coefficients in a Squeeze Film Damper With a Mechanical Seal—Part I: Unidirectional Load Tests," J. Eng. Gas Turbines Power, **129**(3), pp. 858-864.

[24] San Andrés, L., and Delgado, A., 2007, "Identification of Force Coefficients in a Squeeze Film Damper With a Mechanical Seal. Part II—Centered Circular Orbit Tests," J. Tribol., **129**(3), pp. 660-668.

[25] Adiletta, G., and Della Pietra,L., 2006, "Experimental Study of a Squeeze Film Damper With Eccentric Circular Orbits," J.Tribol., **128**(2), pp. 365-377.

[26] Diaz, S., and San Andrés, L., 2001, "Air Entrainment Versus Lubricant Vaporization in Squeeze Film Dampers: An Experimental Assessment of Their Fundamental Differences," ASME J. Eng. Gas Turbines Power, **123**(4), pp. 871-877.

[27] San Andrés, L., 2010, "PW_SFD_2010," SFD Predictive Code developed for Pratt & Whitney Engines, June 2010, Texas A&M University.

[28] San Andrés, L., 2010, "Description of P&W SFD Test Rig (Construction and Operation) and Identification of Test System Parameters (Dry and Lubricated)," Annual Report (Y II) to Pratt & Whitney (United Technologies Corporation), January.

[29] Delgado, A., 2008, "VTR-SFD CCO code," LabVIEW Virtual Instrument Developed for TRC Vertical SFD test rig.

[30] San Andrés, L., 2009, Monthly Progress Report #12 to Pratt & Whitney (United Technologies Corporation), Technical Report No. 12, November 2009.

[31] San Andrés, L., 2010, Monthly Progress Report #21 to Pratt & Whitney (UnitedTechnologies Corporation),Technical Report No. 21, October 2010.

[32] San Andrés, L., Monthly Progress Report #13 to Pratt & Whitney (United Technologies Corporation), Technical Report No. 13, February 2010.

[33] San Andrés, L., 2010, "Identification of Force Coefficients for Two Open Ends SFD Configurations: Long and Short journals," Mid-Year Report 2010 to Pratt & Whitney (United Technologies Corporation), July 2010.

[34] San Andrés, L. and Vance, J., 1987, "Effect of Fluid Inertia on Squeeze Film Damper Forces for Small Amplitude Circular Centered Motions," ASLE Transactions, **30**, pp. 69-76.

[35] San Andrés, L., 2011, "Experimental and Predicted Force Coefficients for Long and Short SFDs: Open and Sealed ends," Annual Report (Y III) to Pratt & Whitney UTC, January.

[36] San Andrés, L., 2010, "Thermal Analysis of Finite Length Journal Bearings Including Fluid Inertia Effects," Modern Lubrication Theory, Notes 7, Texas A&M University Digital Libraries, https://repository.tamu.edu/handle/1969.1/93197 [02/05/2011].

[37] Graviss, M., 2005, " The Influence of a Central Groove on Static and Dynamic Characteristics of an Annular Liquid Seal with Laminar Flow," M.S. Thesis, Texas A&M University, College Station, TX.

APPENDIX A

LIST OF TEST INSTRUMENTATION AND GAINS

The test rig uses eighteen sensors to measure various operation parameters. The sensors comprise of displacement eddy current sensors, accelerometers, load cells, pressure sensors and thermocouples. Table A. 1 lists the sensor names, manufacturer, sensitivities, measurement range and use in the test rig [28].

Table A. 1 List of sensors used in the SFD test rig

Sensor	Manufacturer	Model	Sensitivity	Measurement variable
Eddy current (2) (short damper) REBAM® Eddy current (2) (long damper)	Bently-Nevada®	3300 XL (short damper) 7200 series (long damper)	7.953 V/m [with correlation factors], 39.37 V/m (REBAM)	Bearing cartridge displacement with respect to journal along X and Y axes
Accelerometer (2)	PCB®	353B33	106 mV/g	Bearing accelerations along X and Y axes
Piezoelectric pressure sensor (6)	PCB®	111A24 and 111A26	72.5 mV/bar and 145 mV/bar	Dynamic pressure in groove (2), upper film land (2) and lower film land (2)
Piezoelectric Load cell (2)	PCB®	208C03	2.24 mV/N	Dynamic load on bearing cartridge applied by shakers along X and Y directions
Strain-gage type pressure transducer (1)	Omega®	PX313-100G5V	0.725 mV/bar	Inlet pressure of lubricant in supply line before entering journal
Strain gage type load cell (1)	Omega®	LC213-500	8.99 mV/kN	Magnitude of static load applied on bearing cartridge to generate off-centered operation
Thermocouple (3)	Omega®	K type	0.072 mV/^{o}C	Temperature of lubricant at journal inlet, exit of top and bottom lands
Flowmeter (1)	Omega®	FTB791	-	Lubricant flow rate into journal

APPENDIX B

UNCERTAINTY ANALYSIS

This appendix presents the procedure to determine uncertainty in measurements and in the estimation of force coefficients. The uncertainty of a single measurement using a single measuring device is half the least count of the device. The ensuing section explains the measurement uncertainty arising from measurements made using the test rig instrumentation [32].

Uncertainty in displacement measurements

For the short length damper configuration, Bently Nevada® 3300 series eddy current sensors are used to measure the BC displacements with respect to the stationary journal (B). The sensitivity of the eddy current sensors, originally 7.953 V/mm, changes in the presence of extraneous metal close to their sensing tip, hence necessitating a recalibration against reference displacement sensors. The sensitivities of the eddy current sensors along X and Y directions, taking into account the recalibration factors, are 5.718 V/mm and 5.049 V/mm, respectively. The DAQ system saves the sensor voltage to a precision of 1 mV, thus rendering an uncertainty of $\pm$ 1 mV in voltage measurement. This translates to uncertainties of $U_{\delta X} =$ 0.203 μm for and $U_{\delta Y}$=0.178 μm for the X and Y eddy current sensors, respectively.

The long damper uses REBAM® eddy current sensors to overcome the recalibration issue outlined above. Both REBAM® sensors have a sensitivity of 39.37 V/mm, and due to the DAQ system storing voltages to a thousands precision, possess an uncertainty of U_{δ}= 0.025 μm.

Uncertainty in force measurements

The dynamic load cell sensitivities are 2.248 mV/N, translating to an uncertainty of U_F = 0.445 N. The static load cell displays the measured force with a single digit precision, leading to an uncertainty of U_{LS} = ±4.45 N.

Uncertainty in frequency measurement

The resolution of frequency measurements is the ratio of the sampling rate to number of samples. For the short damper, the sampling rate is set at 4096 samples/second, storing 4096 samples, hence the uncertainty in frequency is U_ω=1 Hz (6.3 rad/s). For the long damper, the DAQ reads 16,384 samples/second, storing 4,096 samples, and hence , U_ω=4 Hz (25.1 rad/s).

The following relations are used to determine uncertainties of the estimated mechanical parameters of the system

$$K = \frac{F}{\delta}$$

$$H = F\delta^{-1}$$

$$C = \frac{\text{Im}(H)}{\omega}$$ (B.1)

$$M = \frac{K - \text{Re}(H)}{\omega^2}$$

where $(K, F, \delta, H, C, M, \omega)$ are the stiffness, applied force, displacement, impedance, damping coefficient, inertia coefficient and operating frequency.

Using the Kline-McClintock procedure, the uncertainty U_g of a measurement $g\left(z_1 \quad z_2 \quad ...z_N\right)$ is

$$U_g = \sqrt{\left(\frac{\partial g}{\partial z_1}\right)U_{z_1}^2 + \left(\frac{\partial g}{\partial z_2}\right)U_{z_2}^2 + ...\left(\frac{\partial g}{\partial z_N}\right)U_{z_N}^2}$$

(B.2)

where $U_{z_1}, U_{z_2}, ...U_{z_N}$ are the individual uncertainties for the input parameters. The uncertainties in stiffness, impedance, damping and added mass coefficients, denoted by (U_K, U_H, U_C, U_M), are determined from Eqs.(B.1) and (B.2) as follows

$$\left(\frac{U_K}{K}\right) = \sqrt{\left(\frac{U_F}{F}\right)^2 + \left(\frac{U_\delta}{\delta}\right)^2}$$

$$\left(\frac{U_H}{H}\right) = \sqrt{\left(\frac{U_F}{F}\right)^2 + \left(\frac{U_\delta}{\delta}\right)^2}$$

$$\left(\frac{U_C}{C}\right) = \sqrt{\left(\frac{U_H}{H}\right)^2 + \left(\frac{U_\omega}{\omega}\right)^2}$$

$$\left(\frac{U_M}{M}\right) = \sqrt{\left(\frac{U_K}{K}\right)^2 + \left(\frac{U_H}{H}\right)^2 + 2\left(\frac{U_\omega}{\omega}\right)^2}$$

(B.3)

The measurement uncertainties (U_δ, U_F, U_ω) are substituted in Eqs.(B.3) to obtain uncertainties in the estimated physical parameters. Table 8 shows the uncertainties of the parameters expressed as a percentage. The uncertainties are highest for the lowest test frequency and the smallest amplitude of motion, and decrease rapidly at higher test frequencies and larger amplitudes of motion. For the short damper, the uncertainties for damping and added mass coefficients range from 1.3 - 20.1% and 1.3- 28.4 %, respectively; for the long damper, the corresponding uncertainty ranges are 1.9- 3.6% and 2.7 – 5.1% respectively. The uncertainties of estimated parameters at intermediate test frequencies evidently lie within the aforementioned percentage bounds [24].

Note that the uncertainty for the short length damper coefficients at lowest test frequency (5 Hz) are high (>20%), and rapidly decrease with test frequency. For

example, the uncertainties in the damping and inertia coefficients drop to 4.3% and 6.1% at 35 Hz.

Note that variability of the data cannot be determined because most tests were conducted only once.

Table 8. Uncertainties of estimated parameters for short length and long dampers

	Short length damper		Long damper	
Test frequency	5 Hz	95 Hz	110 Hz	210 Hz
Frequency (U_ω/ω)	20%	1%	3.6%	1.9%
Displacement (U_δ/δ)	1.6%	0.8%	3.6%	1.9%
Force (U_F/F)	0.10%	0.03%	0.05%	0.03%
Stiffness (U_K/K)	1.6%	0.8%	0.5%	0.1%
Impedance (U_H/H)	1.6%	0.8%	0.5%	0.1%
Damping coefficients (U_C/C)	20.1%	1.3%	3.6%	1.9%
Inertia coefficients (U_M/M)	28.4%	1.8%	5.1%	2.7%

VITA

Name: Sanjeev Seshagiri

Address: Department of Mechanical Engineering, 3123 TAMU,

                 College Station, TX 77843, USA

                 C/O Dr. Luis San Andrés

Email: SanjeevSeshagiri@gmail.com

Education: B.E, Mechanical Engineering, R.V.College of Engineering,

                 Bangalore, India , 2007

                 M.S, Mechanical Engineering, Texas A&M University, 2011